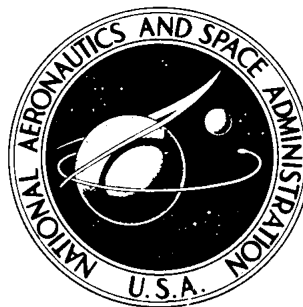


NASA TECHNICAL NOTE



NASA TN D-4813

NASA TN D-4813

FLOW-FIELD INVESTIGATIONS ON THE X-15 AIRPLANE AND MODEL UP TO HYPERSONIC SPEEDS

by L. J. McLain and Murray Palitz

Flight Research Center

Edwards, Calif.

NATIONAL AERONAUTICS AND SPACE ADMINISTRATION • WASHINGTON, D. C. • SEPTEMBER 1968

FLOW-FIELD INVESTIGATIONS ON THE X-15 AIRPLANE
AND MODEL UP TO HYPERSONIC SPEEDS

By L. J. McLain and Murray Palitz

Flight Research Center
Edwards, Calif.

NATIONAL AERONAUTICS AND SPACE ADMINISTRATION

For sale by the Clearinghouse for Federal Scientific and Technical Information
Springfield, Virginia 22151 - CFSTI price \$3.00

FLOW-FIELD INVESTIGATIONS ON THE X-15 AIRPLANE AND MODEL UP TO HYPERSONIC SPEEDS

By L. J. McLain and Murray Palitz
Flight Research Center

SUMMARY

Flight-measured impact pressures and local Mach numbers near the surface of the rear-lower-fuselage centerline, wing lower surface, and upper vertical tail of the X-15 airplane are presented and compared with calculated results and wind-tunnel data. In addition, wind-tunnel-derived total pressures in the rear-lower-fuselage flow field are presented. The flight measurements are presented over a free-stream Mach number range of 1 to 5.7 and an angle-of-attack range of 0° to 20° . The wind-tunnel measurements cover a Mach number range of 4.0 to 8.0.

The calculated predictions of Moeckel-Love and Inouye-Lomax at an angle of attack of 0° gave reasonable estimates of the flight-measured flow-field parameters in the three local-flow regions. Flight-measured impact pressures near the rear lower fuselage were somewhat lower than wind-tunnel measurements, whereas the flight and wind-tunnel measurements for the vertical tail and wing lower surface showed good agreement.

INTRODUCTION

One of the major objectives of the X-15 research program was to provide high-velocity aerodynamic data on an airborne vehicle. To accomplish this objective, extensive flight and wind-tunnel investigations of the local flow around the vehicle were conducted. Flight data from these investigations in the form of surface pressure coefficients for the forward fuselage, wing, and vertical tail are presented in references 1 to 3, respectively. The results from similar wind-tunnel investigations are presented in references 4 to 6. Flight and wind-tunnel flow-field measurements obtained along the lower centerline of the ogive section of the fuselage up to approximately 32.5 nose diameters downstream of the nose are presented in reference 7. Some local Mach number measurements obtained in flight on the lower surface of the wing and upper-vertical-tail surfaces of the X-15 are included in references 8 and 9, respectively. Schlieren photographs are analyzed in reference 10 in order to determine the flow field in the rear-lower-fuselage region. Results of wind-tunnel tests of the lower-fuselage flow field at the Arnold Engineering Development Center are presented in references 11 and 12.

This paper presents and analyzes additional wind-tunnel and flight flow-field parameters on the X-15 airplane. The regions investigated include the rear lower

fuselage, the lower surface of the wing, and the upper vertical tail. Flight impact and static pressures and Mach numbers at two stations along the lower surface of the fuselage are compared with wind-tunnel data and calculated values. Similar comparisons are made for two upper-vertical-tail configurations and for several positions on the lower surface of the right wing.

The flight data extend through the boundary layer to 12 inches (30.5 centimeters) from the local aerodynamic surface and cover a Mach number range of 1.0 to 5.7 and Reynolds numbers varying from 0.2×10^6 to 2.0×10^6 per foot (0.655×10^7 to 6.55×10^7 per meter). The corresponding wind-tunnel data also extend well past the boundary layer and cover a Mach number range of 4.0 to 8.0 at a Reynolds number of approximately 3.5×10^6 per foot (1.15×10^7 per meter).

SYMBOLS

b_{vt}	span of the upper vertical tail, 83 in. (211 cm) (fig. 2(b))
c	chord length, in. (cm)
c_{vt}	length used to normalize vertical-tail rake positions, 100 in. (254 cm)
D	maximum fuselage diameter, excluding external fairings, 56 in. (142 cm)
d	diameter of leading edge of blunt-leading-edge tail, 1.0 in. (2.54 cm)
l	length of airplane, 594 in. (1510 cm)
M	Mach number
p	static pressure, lb/sq ft (N/sq m)
p_i	impact pressure (total pressure behind normal shock), lb/sq ft (N/sq m)
p_s	surface static pressure, lb/sq ft (N/sq m)
p_t	total pressure, lb/sq ft (N/sq m)
q	dynamic pressure, $0.7 M^2 p$, lb/sq ft (N/sq m)
r	wing leading-edge radius, in. (cm)
x	distance measured longitudinally along aircraft surface, in. (cm)
y	distance measured laterally along aircraft surface, in. (cm)
z	distance measured vertically from datum, in. (cm)
α	angle of attack, deg
β	angle of sideslip, deg

γ specific-heat ratio, 1.4
 φ circumferential angle on fuselage (fig. 2(a)), deg

Subscripts:

l local conditions (within the flow field)
 ∞ free-stream conditions

AIRPLANE AND MODEL DESCRIPTION

Airplane

The X-15 is a single-place, rocket-powered, research airplane capable of speeds in excess of 6000 feet/second (1.83 kilometers/second) and altitudes greater than 300,000 feet (91.4 kilometers). It is launched from a B-52 carrier aircraft at a Mach number of 0.8 and an altitude of about 45,000 feet (13.7 kilometers). A photograph of the airplane is shown in figure 1. The forward fuselage consists of a spherical-nose

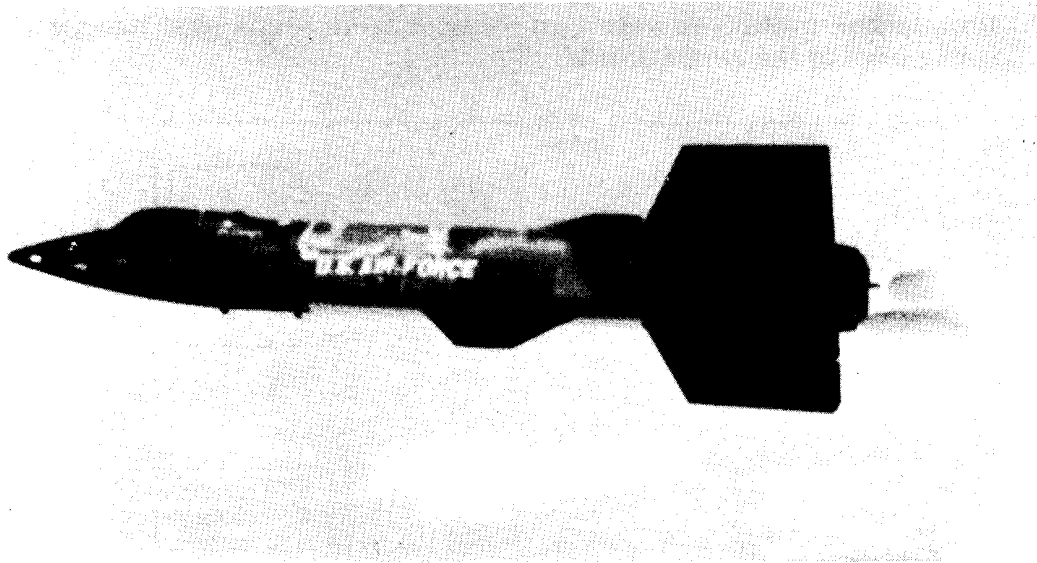


Figure 1.— X-15 airplane in flight.

ES 2118

flow-direction sensor faired into an ogive forebody through two truncated cones (ref. 13). The ogive is generated from the arc of a 700-inch- (17.8-meter-) radius circle which intersects the second truncated cone 16.7 inches (42.4 centimeters) behind the nose (fig. 2(a)) and is tangent to the cylindrical fuselage at a rearward distance of 190 inches (483 centimeters). Two leading-edge configurations on the upper vertical tail were used for these tests: a (sharp) 0.030-inch- (0.076-centimeter-) diameter leading edge, and the normal (blunt) 1.0-inch- (2.54-centimeter-) diameter leading edge (ref. 9). Each leading-edge configuration was faired into a 10° included-angle wedge. The

exposed wing panel has a modified NACA 66005 airfoil section with a taper ratio of 0.27 and an aspect ratio of 2.15. The leading edge is swept back 36.75° , and the trailing edge is swept forward 17.74° .

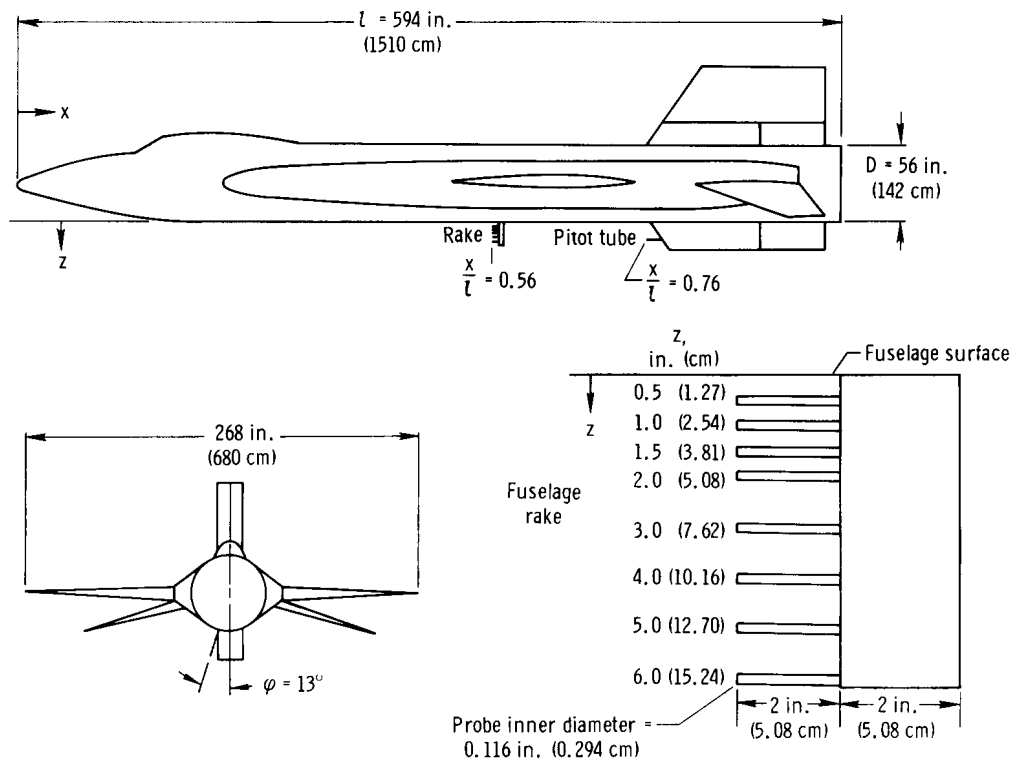
Model

The 0.067-scale heat-transfer and pressure model of the X-15 was used for most of the wind-tunnel tests. Limited tests were also made with a 0.02-scale model. A detailed description of the model is given in reference 5. In addition to the blunt leading edge, a sharp leading edge was used on the vertical tail during the $M_\infty = 4.7$ tests.

INSTRUMENTATION

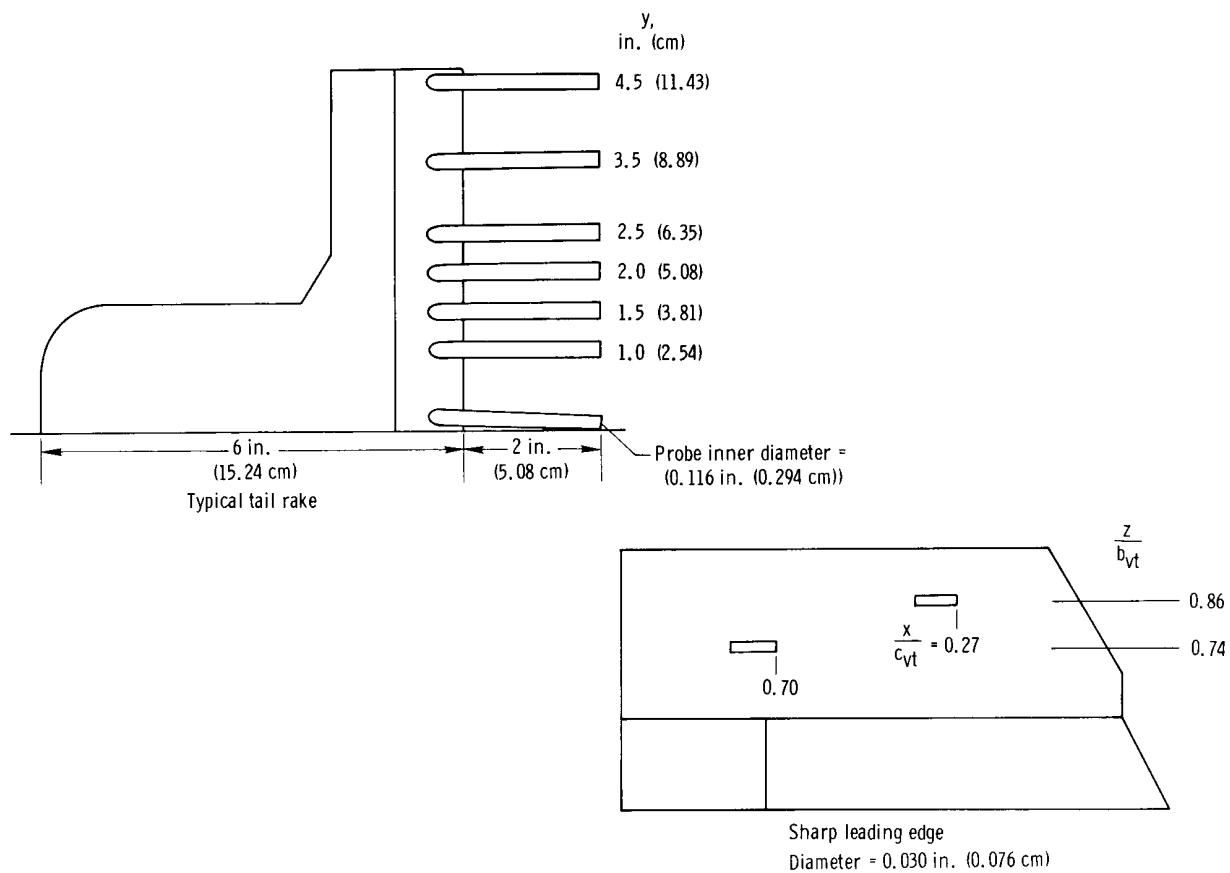
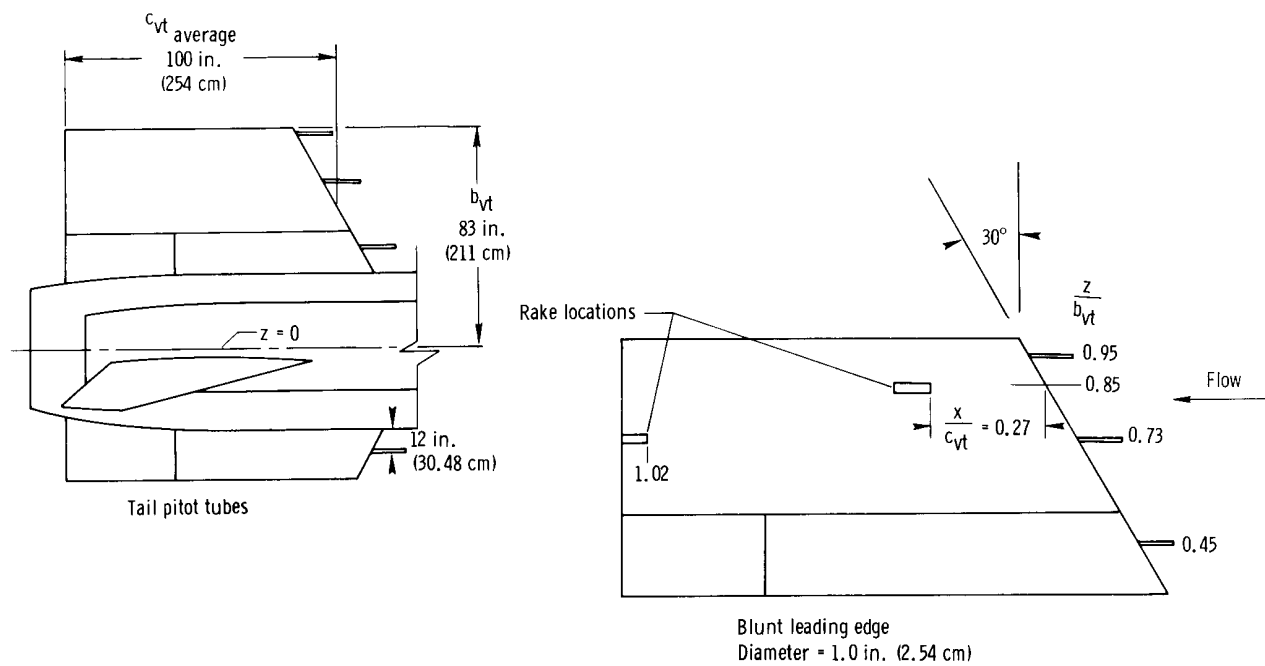
Flight

The airplane rake and pitot-tube installations are shown in figures 2(a) to 2(c). The rakes were constructed from Inconel tubing sandwiched between Inconel plates with either a rounded or a sharp leading edge. Static-pressure orifices flush with the airplane surface were located near the base of the rakes. Aerodynamic design information for the rakes was obtained from wind-tunnel investigations (for example, ref. 14). Impact pressures were also obtained from single pitot tubes extending from the leading edge of the vertical tail.



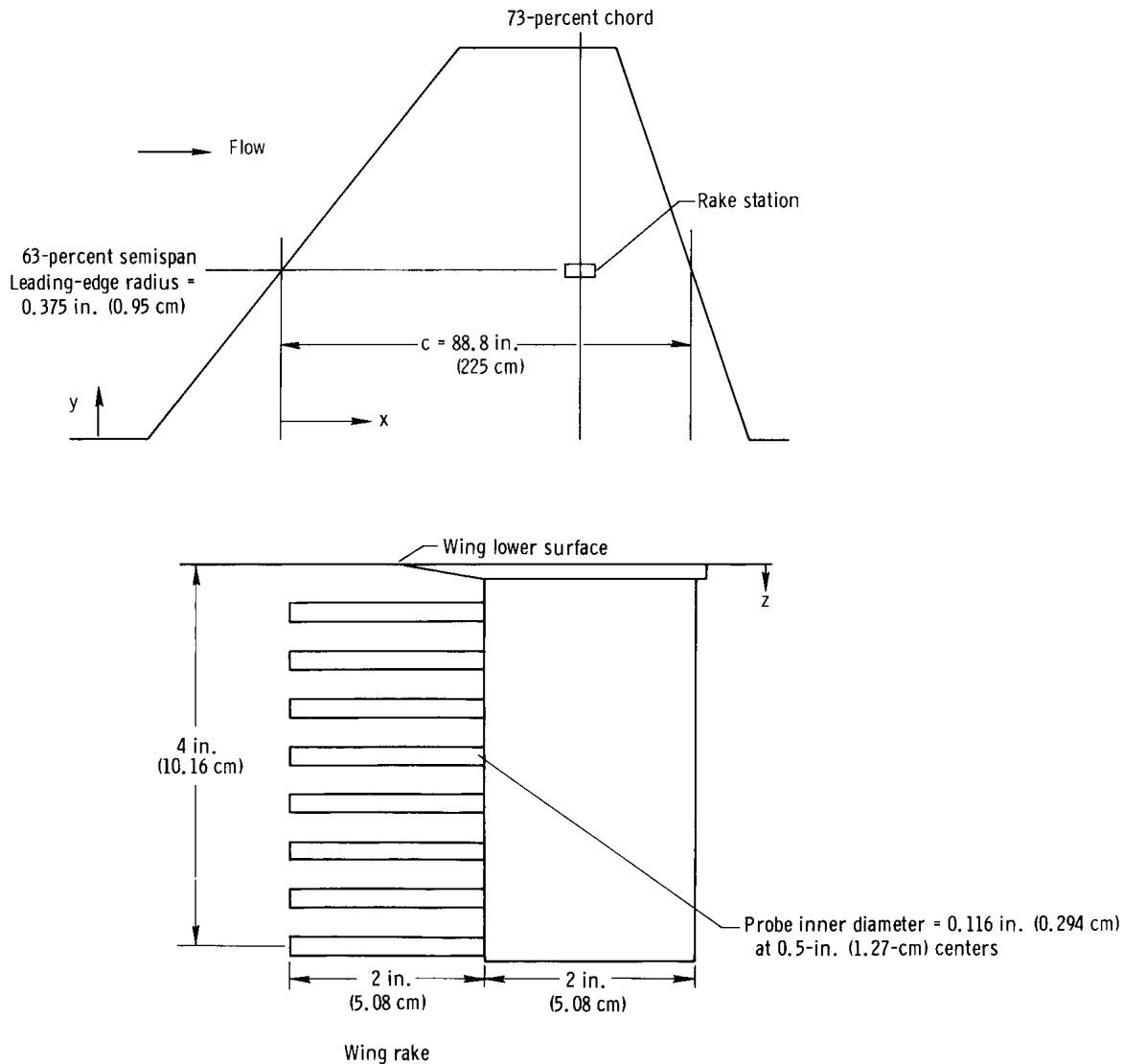
(a) Fuselage.

Figure 2.— Rake and pitot-tube installations on X-15 airplane.



(b) Tail.

Figure 2.— Continued.



(c) Wing lower surface.

Figure 2.— Concluded.

Pressures were recorded on standard NACA aneroid-type manometers. The accuracy of the system was about 1 percent of the full-scale pressure range. The data were generally measured at pressure values near one-half scale, which resulted in an overall accuracy of about 2 percent for individual measurements. Angles of attack and sideslip were obtained from the ball-nose flow-direction sensor, as discussed in reference 13.

Altitude and free-stream velocity were obtained by radar, and free-stream static pressure from balloon ascent data. Both techniques are discussed in detail in references 15 and 16. The estimated accuracy of each air-data parameter was as follows:

Parameter	Estimated accuracy	Source
M_∞	± 0.1	Reference 15
α	$\pm 0.5^\circ$	Reference 13
β	$\pm 0.5^\circ$	Reference 13
p_∞	$\pm 2 \text{ lb/ft}^2$ ($\pm 96 \text{ N/m}^2$)	References 15, 16
p_{i_∞}	$\pm 6 \text{ lb/ft}^2$ ($\pm 287 \text{ N/m}^2$)	References 15, 16

All measurements were correlated with a common timer.

Wind Tunnel

The data presented in this paper were obtained from the Arnold Engineering Development Center's (AEDC) von Karman Gas Dynamics Facility (VKF), Tunnels A and B, and the NASA Langley Research Center's (LRC) Unitary Plan and 11-inch (27.9-centimeter) hypersonic wind tunnels. The tunnel data through $M_\infty = 6.0$ were from the AEDC VKF Tunnel A. The VKF Tunnel B was used to obtain the $M_\infty = 8.0$ data. These tests were made with the 0.067-scale model. Fuselage data and schlieren photographs used to analyze shock positions were obtained from tests of the 0.067-scale model in the Langley Unitary Plan tunnel at $M_\infty = 4.7$. Also, schlieren photographs used to analyze shock positions were obtained with a 0.02-scale model in the Langley 11-inch (27.9-centimeter) supersonic tunnel at $M_\infty = 6.9$. The 0.02-scale model is described in reference 17. The wind tunnels are described in detail in references 18 and 19, and the AEDC instrumentation and test equipment are shown in figures 3(a) to 3(c) and described in reference 12.

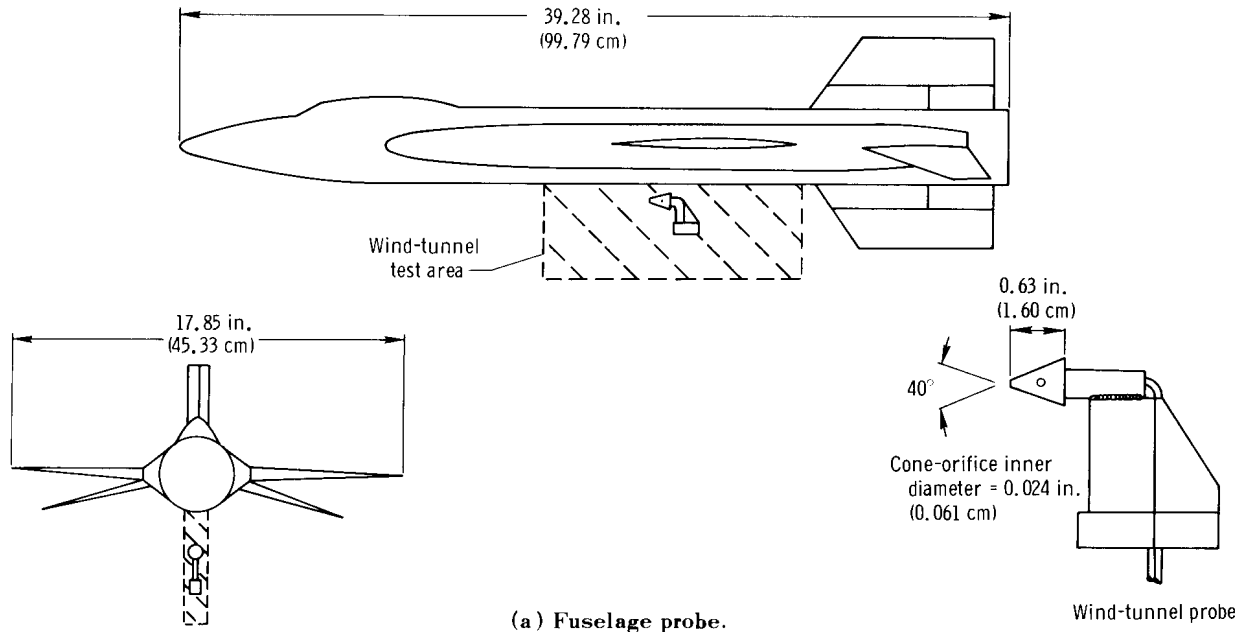
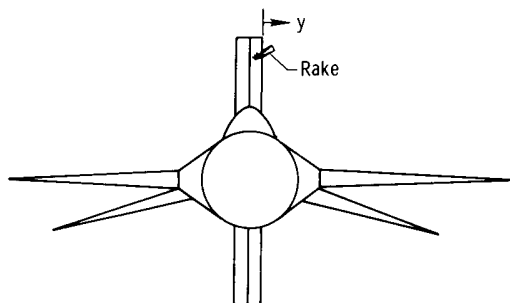
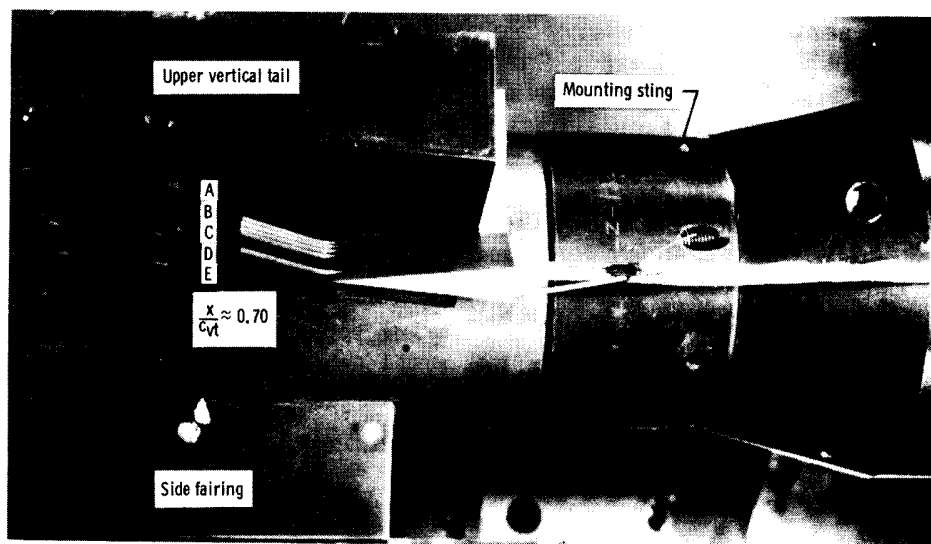


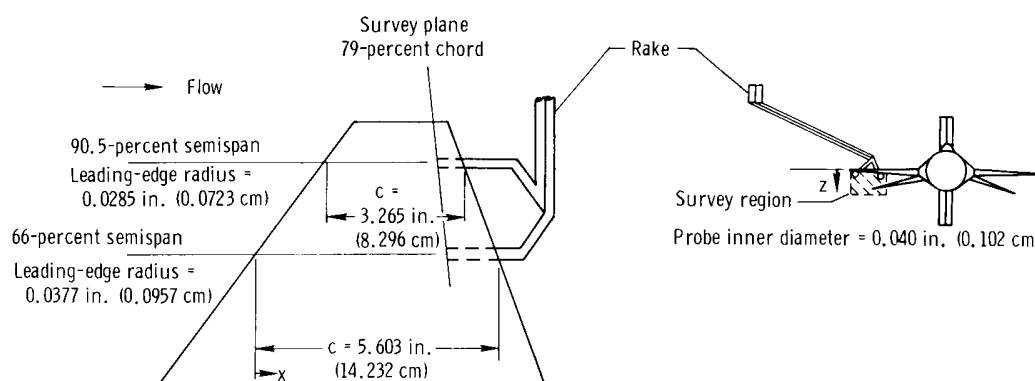
Figure 3.— AEDC wind-tunnel instrumentation on X-15 model.



Probe	y, in. (cm)
A	0.027 (0.069)
B	.100 (.254)
C	.187 (.475)
D	.487 (1.237)
E	1.167 (2.964)



(b) Tail rake.



(c) Wing lower-surface survey for wind-tunnel model.

Figure 3.— Concluded.

TEST CONDITIONS AND PROCEDURES

The flight data were obtained at altitudes up to 120,000 feet (36.6 kilometers) and Mach numbers up to 5.7. The pressure data for the wing and lower fuselage were obtained at quasi-steady flight conditions. At these conditions the rate of change of angle of attack was less than 1 degree per second. The angle of sideslip was restricted to less than $\pm 1^\circ$. The Reynolds number varied from 0.2×10^6 to 2.0×10^6 per foot (0.655×10^6 to 6.55×10^7 per meter). The rake data on the vertical tail were obtained between airplane angles of attack of $\pm 1^\circ$ and effective tail deflections (sum of the airplane sideslip angle and tail deflection angle) of less than $\pm 1^\circ$. Free-stream dynamic pressures were greater than 200 lb/ft² (9.57 kN/m²) for all conditions.

The wind-tunnel test conditions and procedures are discussed in references 11 and 12.

PRESENTATION OF RESULTS

All pressure data are nondimensionalized with respect to free-stream conditions. Static pressures are presented as a ratio of local static pressure p to free-stream static pressure p_∞ and impact pressures as a ratio of local impact pressures p_i to free-stream impact pressures p_{i_∞} , where p_i and p_{i_∞} are the total pressures behind the pitot-tube normal shock in the flow field and free stream, respectively. This approach simplified correlation between flight, wind-tunnel, and theoretical data.

Airplane coordinates are normalized with respect to appropriate characteristic dimensions of the airplane. Model coordinates were converted to equivalent airplane coordinates for the presentation of the model data.

Local Mach numbers were obtained by using the Rayleigh pitot-tube formula based on the surface static pressure and the measured impact pressures in the flow field up to 6 inches (15.24 centimeters) from the surface.

Total-pressure values near the surface were obtained by using the isentropic relationship between local Mach number (derived from impact pressure) and the local static pressure (assumed to be the surface value). The total-pressure values directly behind the bow shock were derived from shock angles, which were obtained from schlieren photographs.

DISCUSSION

Fuselage

Axisymmetric theory.— The basic shape of the X-15 fuselage, excluding canopy, side fairings, and wings, is assumed by theory to be an axisymmetric ogive-cylinder with a spherical nose at the forward stagnation region. The Inouye-Lomax numerical procedure (ref. 20) was used to calculate the flow properties along the ogive-cylinder at zero angle of attack. This procedure uses the Fuller blunt-body solution (ref. 21) to

provide the flow properties in the subsonic and transonic regions around the forward stagnation point. These results are then used as starting conditions for the method-of-characteristics procedure to obtain static pressure, local Mach numbers, total pressure, and other flow properties. The Inouye-Lomax method was shown to adequately predict the flow development over the forward ogive of the X-15 airplane in reference 7. Therefore, this method is also used to predict the flow along the aft (cylindrical) portion of the fuselage.

Local Mach number and normalized static pressures through the flow field at several longitudinal stations along the lower centerline of the cylindrical fuselage, obtained by the Inouye-Lomax procedure, are presented in figure 4. The local Mach number variations from $\frac{z}{D} = 0.1$ to the shock or to a maximum $\frac{z}{D}$ of 1.8 are presented in figure 4(a) at several stations along the fuselage for $M_\infty = 4.0$, 6.0, and 8.0. The local Mach numbers increase above the free-stream Mach numbers at $\frac{x}{l} = 0.757$ for all three free-stream Mach numbers and then decrease as a result of a recompression of the flow field. The local Mach number gradient through the flow field for each fuselage position increases with increase in free-stream Mach number.

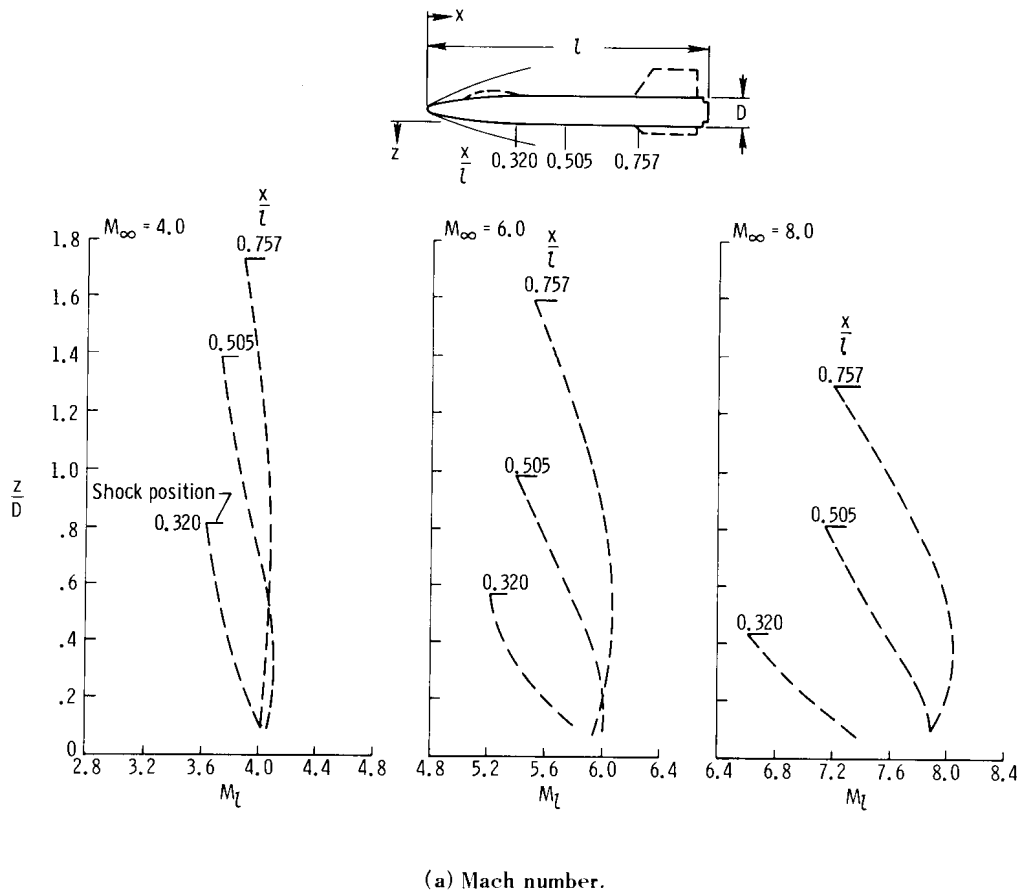
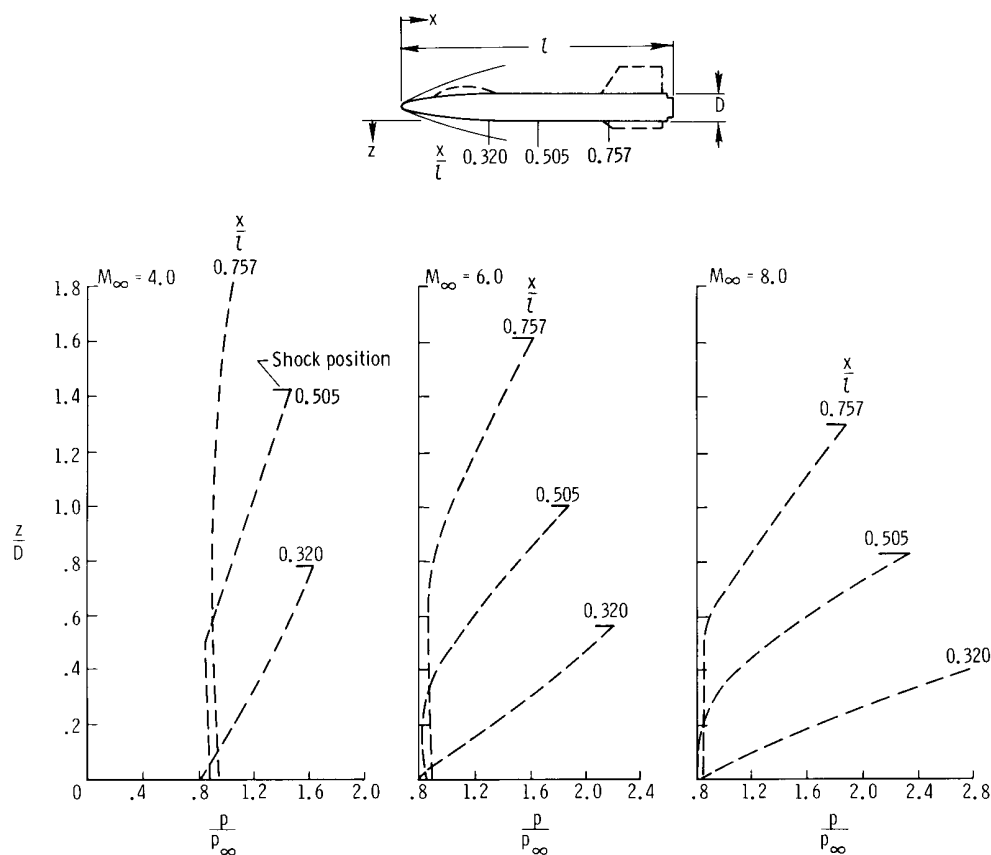


Figure 4.— Variation of Mach number and static pressure through the flow field at $\alpha = 0^\circ$ as predicted by the Inouye-Lomax solution.

The normalized static-pressure variations from the surface to the shock or to a maximum $\frac{z}{D}$ of 1.8 are presented in figure 4(b) at several stations along the cylinder.

The static pressures at $\frac{x}{l} = 0.320$ (ogive-cylinder junction) show a variation through the flow field accompanying the variation of Mach number in this region. It should be noted that the static pressures remain constant to greater distances into the flow field with increasing distance downstream from the ogive-cylinder junction.



(b) Static pressure.

Figure 4.— Concluded.

Wind-tunnel tests.— The 0.067-scale heat-transfer and pressure model was used for these tests. Some of these data were previously reported in reference 12. The present paper includes several additional fuselage stations as well as a comparison with the Inouye-Lomax solutions. The Gallo-Rakich comparisons (ref. 22) as used in reference 12 are also included.

Impact pressure and cone-measured surface static pressures (fig. 3(a)) were obtained from the lower centerline through the flow field at several stations along the rear fuselage. Schlieren photographs were used to obtain the locations of the bow and side-fairing shocks.

Impact-pressure measurements obtained from the surface to a maximum $\frac{z}{D}$ of 1.0 into the flow field are presented in figure 5 for $M_\infty = 4.0, 6.0,$ and 8.0 at 0° angle of attack. The Inouye-Lomax calculations of normalized impact pressure agree with the measurements through the flow field at all the stations shown. The Gallo-Rakich values also show good agreement with the wind-tunnel data at the station at which they are compared. The impact-pressure level from 0.18 diameter to 0.36 diameter from the surface is relatively independent of longitudinal distance over the Mach number range at $\alpha = 0^\circ$. This is believed to result from the constant Mach number and static-pressure levels through this region (fig. 4). The impact pressures beyond 0.36 diameter increase in magnitude, reaching a maximum value at the shock or at the maximum survey height. In addition, the pressure levels through this area decrease as longitudinal distance increases.

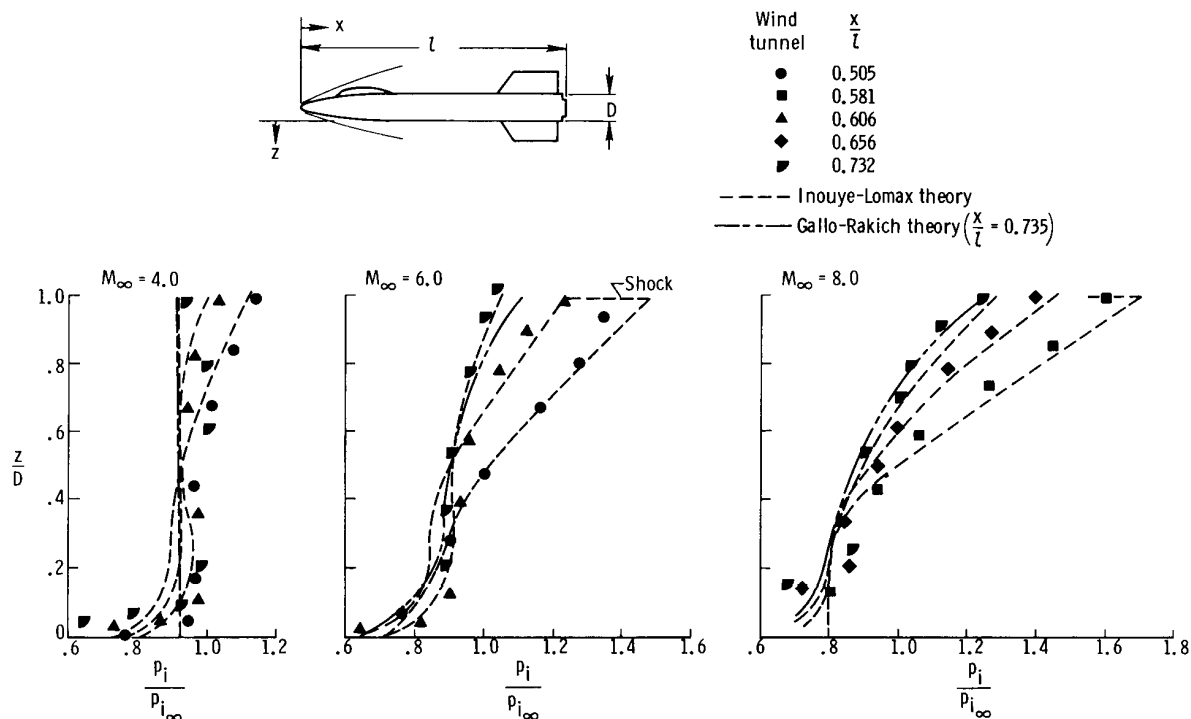


Figure 5.— Variation of normalized impact pressures through the model flow field along the lower centerline.
 $\alpha = 0^\circ$.

The total-pressure variation in the flow field results from the characteristics of the bow-shock shape. The bow-shock angle varies continuously from a value of 90° at the stagnation point of the spherical nose to values approaching the Mach wave many diameters downstream. This variation in shock angle results in the total pressure, within the flow field, varying from a minimum value at the surface to a maximum value directly behind the shock at each cross-sectional location along the aft cylinder.

The embedded shock originating from the side fairings beginning at $\frac{x}{l} = 0.256$ (see ref. 12) causes additional losses in the local total pressures in the flow field. This results in further reduction of the local Mach numbers and an increase in the magnitude of the local static pressure in the regions affected. Total-pressure values obtained from the static and the impact pressures close to the surface (but above the boundary layer) and near the bow shock are presented in figure 6 for $\alpha = 0^\circ$. The data are presented at several stations along the lower centerline and are compared with the Inouye-Lomax and the Gallo-Rakich calculations. The calculated values at $M_\infty = 4.0$ and 6.0 agree with the measurements near the surface and at the shock. The disagreement between the calculations and measurements near the surface at $M_\infty = 8.0$ is thought to be caused by total-pressure losses resulting from the embedded shocks not accounted for by theory. This deviation is not observed for total-pressure values obtained in regions near the bow shock unaffected by the embedded shocks (see ref. 12). Longitudinal distance seems to have little effect on the total-pressure levels.

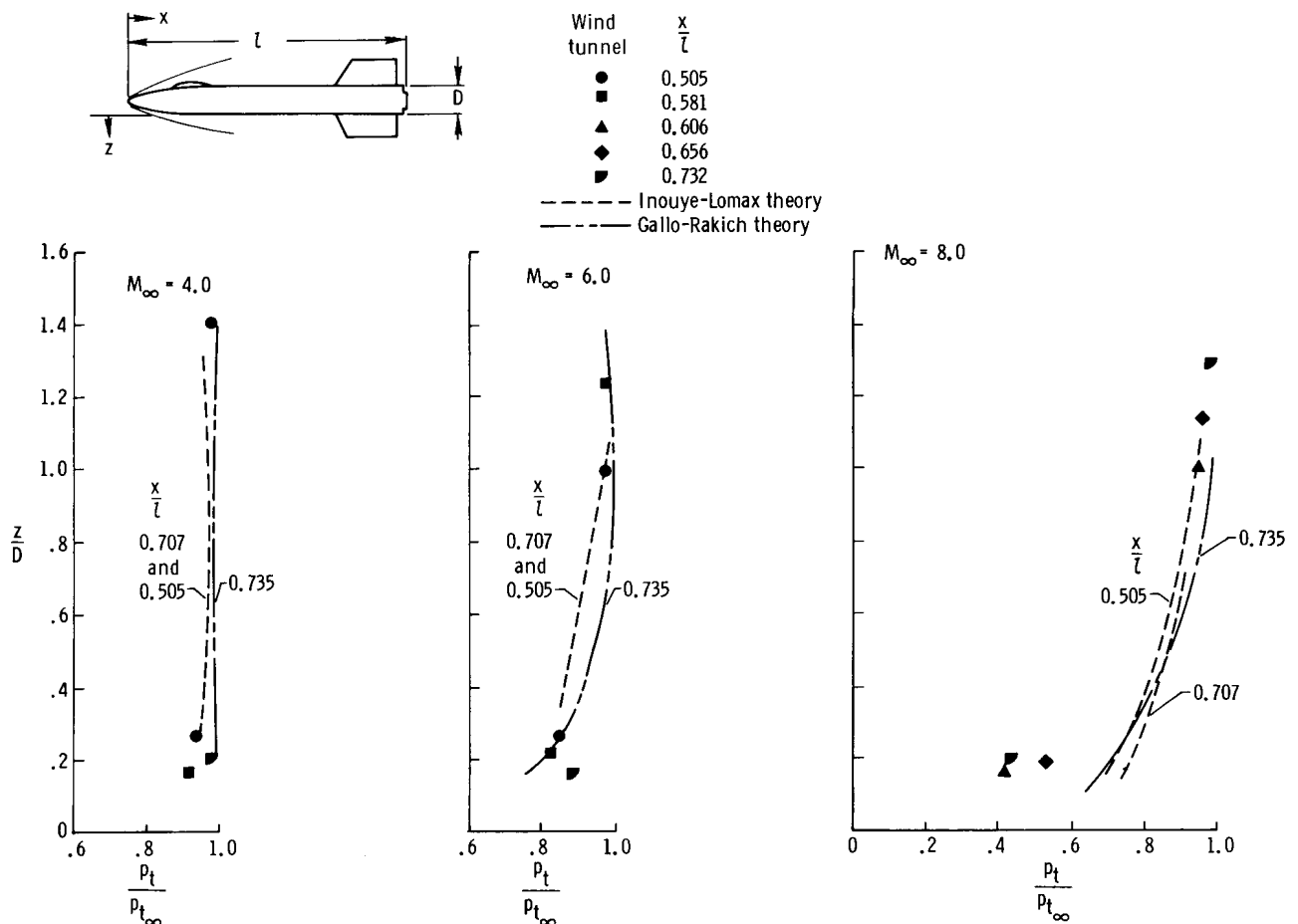
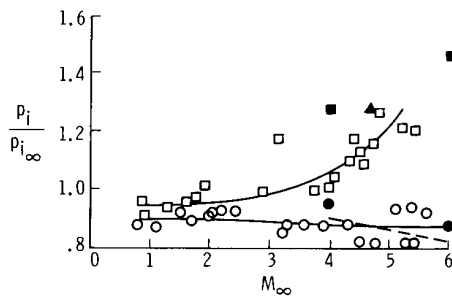
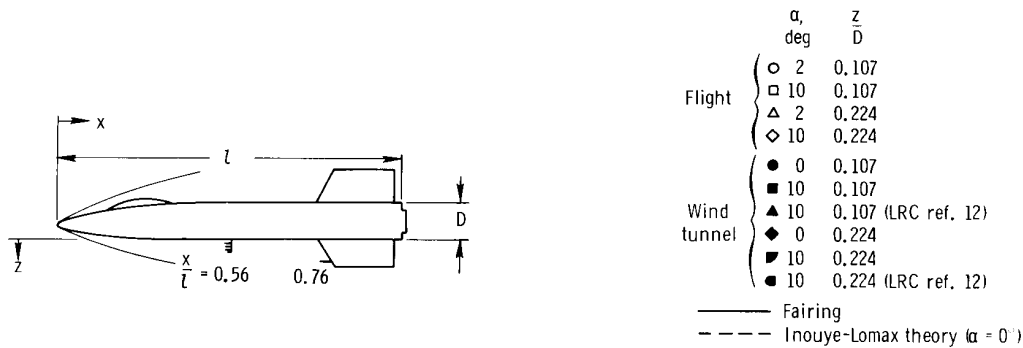


Figure 6.— Variation of total pressure through the model flow field along the lower centerline. $\alpha = 0^\circ$.

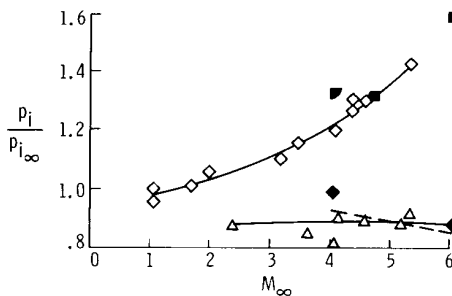
Flight measurements.— Normalized values of impact pressures obtained from the 6-inch (15.24-centimeter) probe of the fuselage rake and the pitot tube in the lower vertical tail (12 inches (30.48 centimeters) below the fuselage) are presented in figures 7(a) and 7(b), respectively, over a free-stream Mach number range of 0.8 to 5.7

at angles of attack of 2° and 10° . The flight data are compared with wind-tunnel data taken along the centerline of the model at comparable distances from the fuselage and with the Inouye-Lomax theory at $\alpha = 0^\circ$.

Considered independently, the wind-tunnel values would indicate higher impact pressures than measured in flight. At both fuselage stations the wind-tunnel data at $M_\infty = 4.0$ are significantly higher than the flight data, whereas the values for the higher Mach numbers show better agreement with the flight data. The general level of the flight data agrees with the Inouye-Lomax solution for $\alpha = 0^\circ$.



(a) Rake impact pressures, $\frac{x}{l} = 0.56$.



(b) Pitot-tube impact pressures, $\frac{x}{l} = 0.76$.

Figure 7.— Comparison of flight measurements along the lower fuselage with wind-tunnel data and theoretical calculations.

The normalized surface static pressure and Mach number values obtained in flight at $\frac{x}{l} = 0.56$ are presented in figures 7(c) and 7(d), respectively, and are compared with equivalent wind-tunnel data and theory. The flight measurements obtained at $\alpha = 10^\circ$ show no appreciable difference from the wind-tunnel data obtained at $\alpha = 10^\circ$. The flight measurements at $\alpha = 2^\circ$ are somewhat different from the wind-tunnel data and Inouye-Lomax theory at $\alpha = 0^\circ$. This variation is attributed to the difference in angle of attack between the flight conditions and the wind-tunnel and theoretical results.

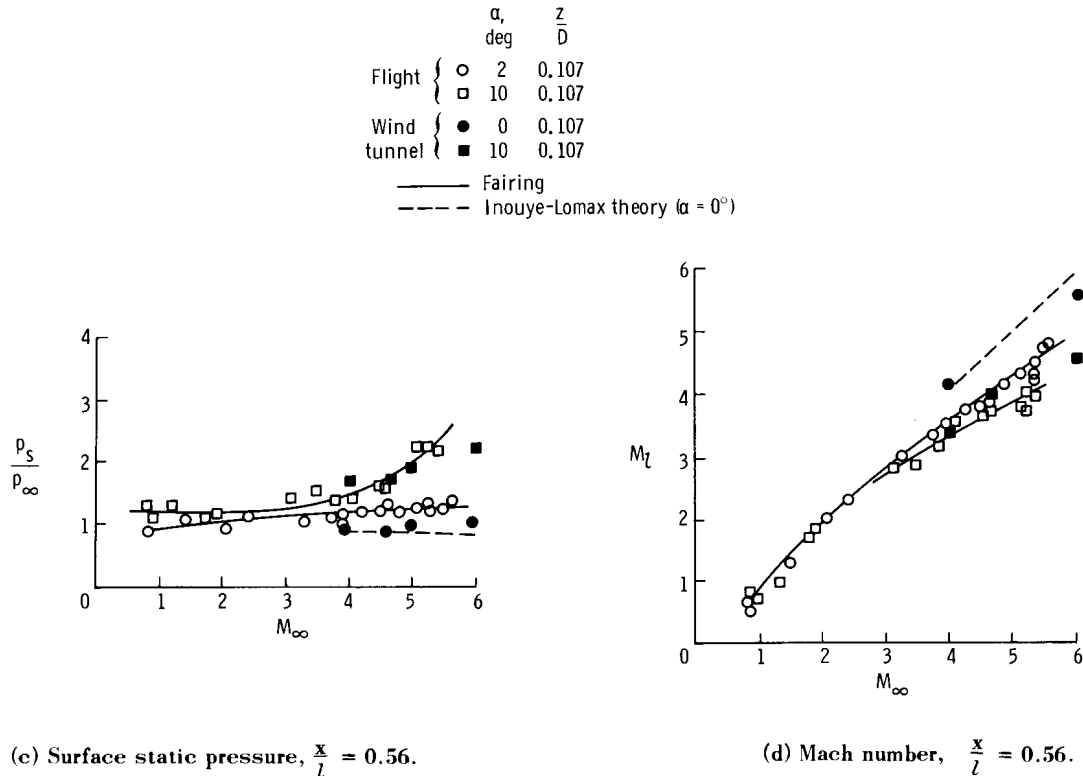


Figure 7.— Concluded.

Vertical Tail

Swept-wedge theory.— The Inouye-Lomax numerical procedure was used to calculate local Mach number and static pressures through the flow field of a 10° swept wedge with the standard (blunt) leading edge. The calculated values extend through the flow field to the shock. The flow field was generated by using the normal component of the free-stream velocity on the equivalent normal wedge shape (half angle = 5.77°). The parallel component of the velocity unaffected by the shock was added to the calculated values for the equivalent wedge.

The normalized static pressures through the flow field at $M_\infty = 4.7$ are presented in figure 8(a) at several longitudinal locations. The effect of increasing longitudinal distance on the static pressures results in a decrease in both the pressure level and the gradient from the surface.

The Mach number values through the flow field are presented in figure 8(b) at two representative stations along the chord. The Mach number level increases with increasing distance downstream as the result of the greater flow expansion downstream of the leading edge. As can be seen in both figures, the oblique-shock calculations adequately predict the local-flow conditions at the $\frac{x}{d} = 50$ station and $\frac{y}{d}$ greater than 5.

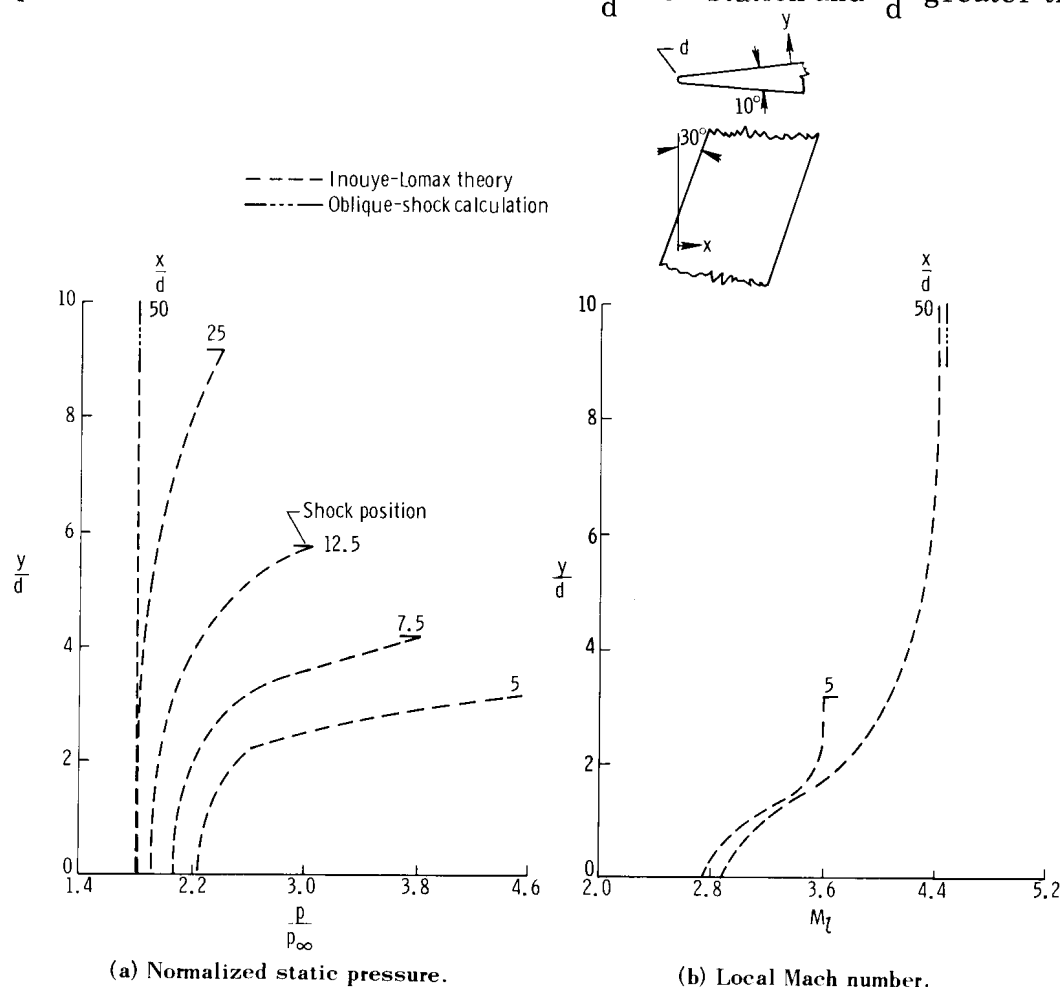


Figure 8.— Theoretical variation of normalized static pressures and Mach number on a swept blunt wedge at $\alpha = 0^\circ$ as predicted by the Inouye-Lomax solution at $M_\infty = 4.7$.

Flight measurements.— The upper vertical stabilizer is located in the flow field affected by the forebody shape. The flow conditions in front of the vertical tail were determined by impact-pressure measurements from pitot tubes extending from the leading edge of the tail at three span positions (fig. 2(b)).

The normalized impact-pressure values can be shown to approximate normalized dynamic-pressure values $\frac{q}{q_\infty}$ (see appendix). The normalized dynamic pressures provide some indication of the flow gradients in this region. The blunt-vertical-tail data are presented as functions of free-stream Mach number and angle of attack at constant span locations in figures 9(a) to 9(c). Local dynamic-pressure values decrease near the leading edge of the vertical tail with increasing α or M_∞ . At the higher angles of attack, the blanketing effect of the canopy and fuselage on the flow causes a decrease

in total pressure and, consequently, a decrease in the local dynamic pressure. At a constant α the local dynamic pressures decrease as Mach number becomes greater. This decrease is attributed to the total-pressure losses in passing through the stronger bow and canopy shocks. For constant M_∞ and α , the local dynamic pressure increases with distance from the fuselage. The gradient in dynamic pressure decreases with distance from the fuselage for any given Mach number.

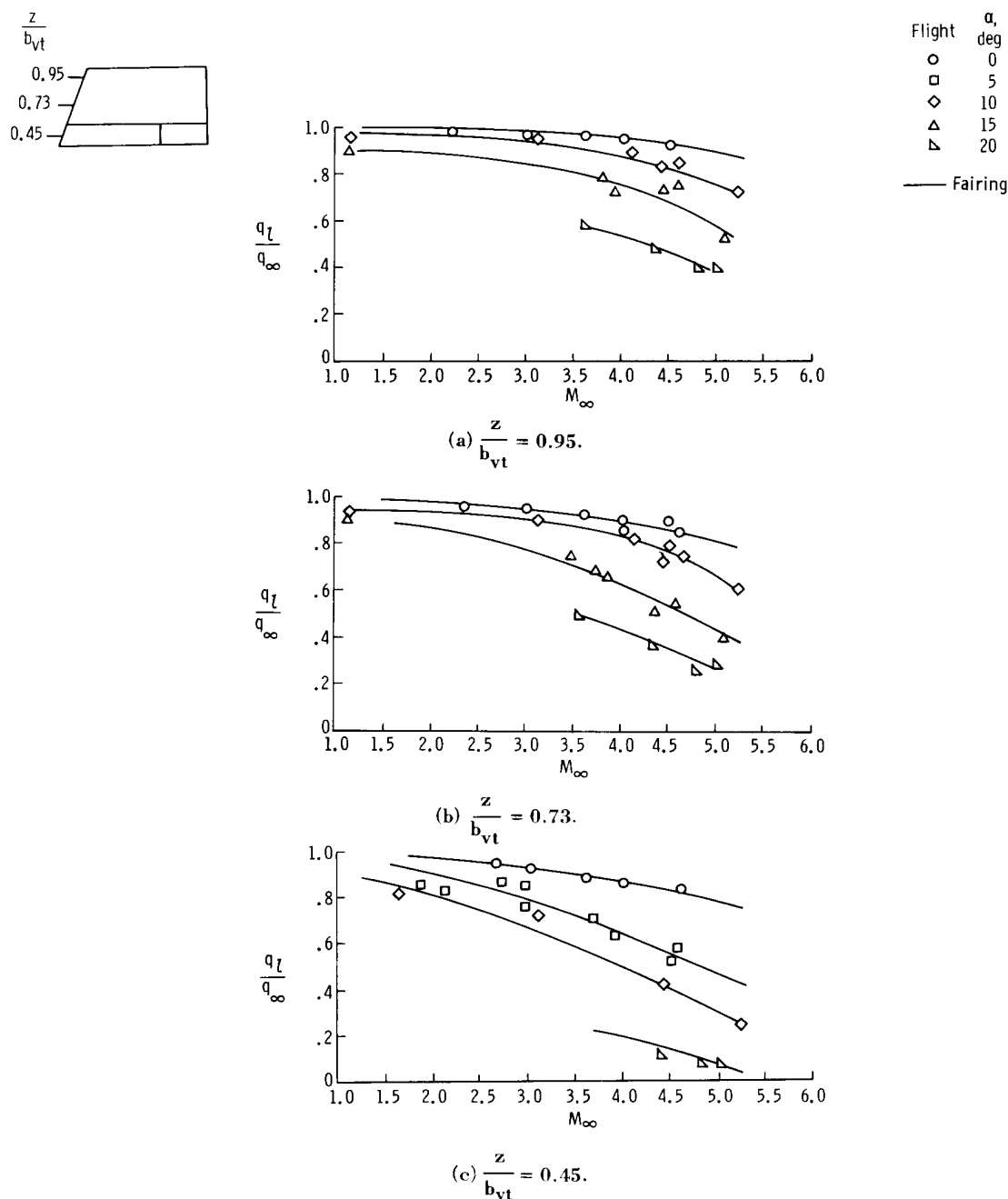


Figure 9.— The effect of free-stream Mach number and angle of attack on the local dynamic pressures in front of the blunt upper vertical tail at three span locations in flight.

Normalized impact-pressure measurements obtained from rakes installed at two chord positions on the surface of the sharp-leading-edge upper vertical tail and two chord positions on the blunt-leading-edge vertical tail are presented in figure 10. The data are presented as a function of free-stream Mach number for constant tube heights from the surface at zero angle of attack. The normalized impact-pressure data for the sharp-leading-edge configuration are presented in figure 10(a). The flight data show good agreement with the wind-tunnel results and no apparent effect of chord or span positions. The data indicate that no gradient along the probe exists at either position up to $M_\infty = 4.7$ at distances beyond 1.5 inches (3.81 centimeters) from the surface. The reduction in impact pressures below this height is attributed to boundary-layer growth along the wedge surface (ref. 9). The boundary-layer thicknesses are estimated to vary from 0.439 inch (1.115 centimeters) at $\frac{x}{c_{vt}} = 0.27$ to 1.37 inches (3.48 centimeters) at $\frac{x}{c_{vt}} = 0.90$ for $M_\infty = 2$, and from 0.37 inch (0.94 centimeter) at $\frac{x}{c_{vt}} = 0.27$ to 1.19 inches (3.02 centimeters) at $\frac{x}{c_{vt}} = 0.90$ for $M_\infty = 4.0$.

Normalized impact pressure data for the blunt-edge configuration are presented in figures 10(b) and 10(c). The data at both chord positions show a gradient from

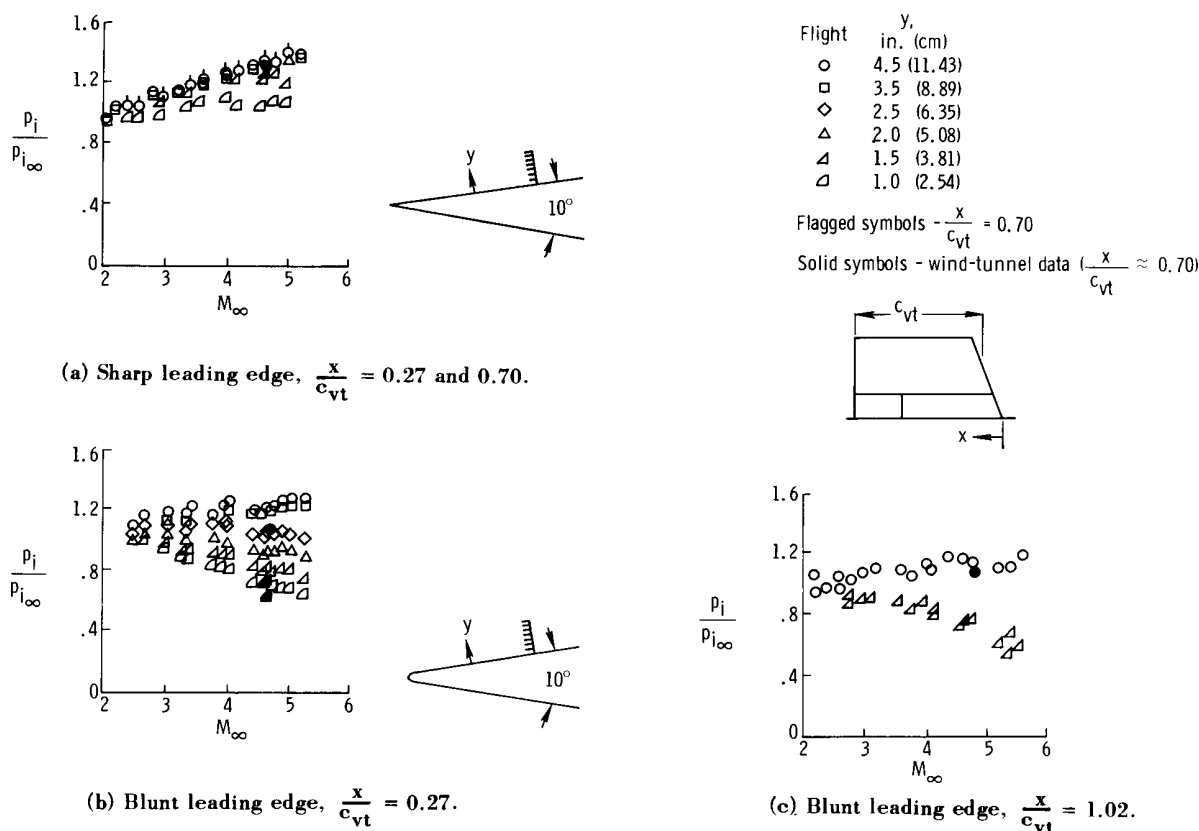


Figure 10.— Effect of free-stream Mach number on the normalized impact pressures on the upper vertical tail at $\alpha = 0^\circ$ in flight.

1.0 inch to 4.5 inches (2.54 centimeters to 11.43 centimeters) from the surface. The gradient increases with increasing Mach number. The pressure-level difference between the two locations is believed to be partially due to the difference in lateral location (see fig. 9). The wind-tunnel data for $M_\infty = 4.7$, obtained at $\frac{x}{c_{vt}} \approx 0.70$, compare well with the flight data at $\frac{x}{c_{vt}} \approx 1.02$ but deviate from the flight data obtained at $\frac{x}{c_{vt}} \approx 0.27$. This deviation is attributed to the differences in chord positions.

Local Mach numbers derived from the flight-measured impact and surface static pressure are presented in figure 11 at $M_\infty = 5.0$. The data obtained are shown in figure 11(a) for the blunt- and the sharp-leading-edge configurations. The local Mach numbers through the flow field are compared with results obtained from the Inouye-Lomax solution and the simpler Moeckel-Love method¹ as well as the attached oblique-shock calculations. The local Mach numbers obtained on the sharp-leading-edge configuration compare well with the values obtained from the oblique-shock calculations above the boundary layer. The Inouye-Lomax and Moeckel-Love methods predict the level and trend of the data obtained on the blunt-leading-edge configuration. The effect of chord position is shown in figure 11(b). A greater effect of chord position is

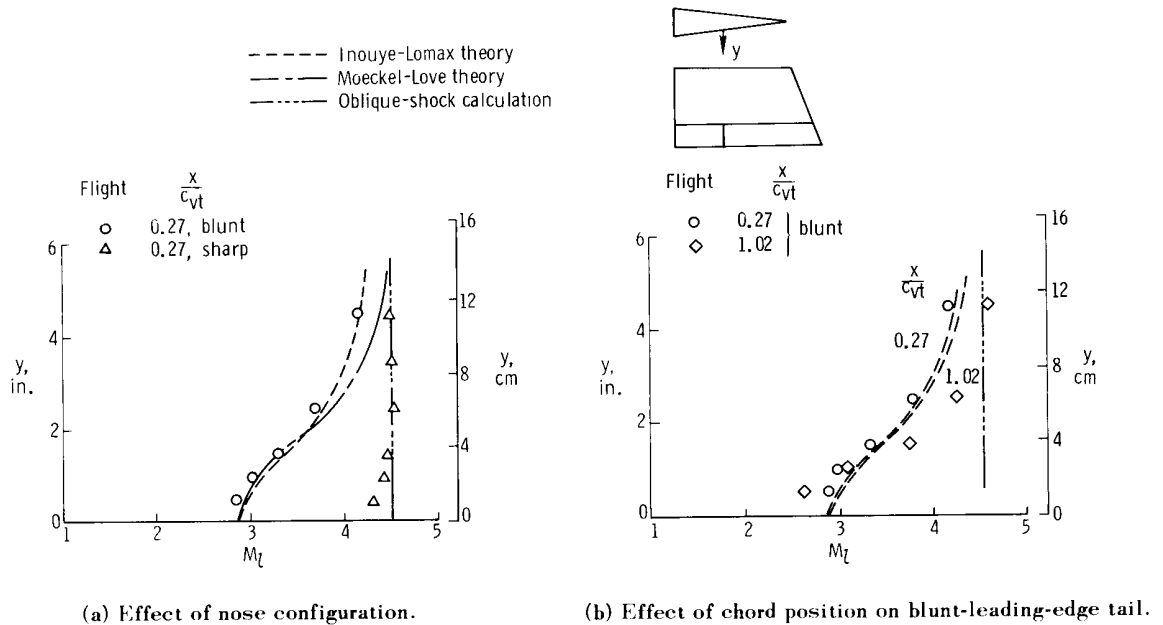


Figure 11.— Comparison of flight-measured upper-vertical-tail local Mach number profiles with theory at $M_\infty = 5.0$, $\alpha = 0^\circ$.

¹The Moeckel-Love numerical procedure used to calculate Mach number profiles in the shear layer for detached shock waves is outlined in reference 23. The procedure is based on Moeckel's method (ref. 24) with Love's modification for predicting the sonic point on the shock wave (ref. 25). The method is used to predict the local Mach number in areas where the surface static-pressure values are known and are assumed to remain at the surface static values for small distances above the surface.

apparent in the flight data than in the predicted values. The deviation is attributed to disturbances originating from the leading-edge tip and junction of the leading edge and the fuselage of the vertical tail.

Local Mach numbers over the Mach number range tested are presented in figures 12(a) and 12(b). The derived Mach number values for the sharp leading edge are compared with the oblique-shock calculations in figure 12(a) and show good agreement. In general, the flight data for the blunt leading edge (fig. 12(b)) agree with the Moeckel-Love calculations at all probe heights. The flight data show good agreement with the oblique-shock calculation for the blunt leading edge at $\frac{x}{c_{vt}} = 1.02$ and $y = 4.5$ inches (11.4 centimeters).

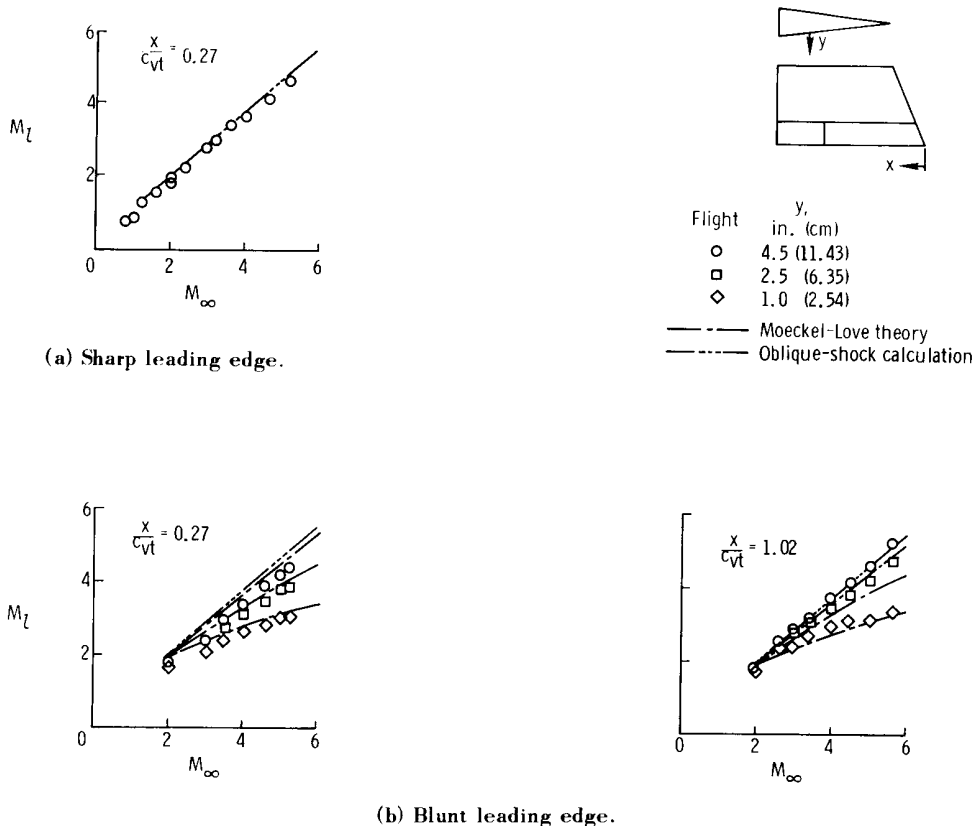


Figure 12.— Comparison of flight-measured local Mach number on the upper vertical tail with calculated results at $\alpha = 0^\circ$.

Wing

Swept-airfoil theory.— The Inouye-Lomax numerical procedure was used to calculate the flow conditions around an airfoil section having the same cross-sectional shape as the X-15 wing. The free-stream Mach number component normal to the leading edge was used to generate the flow field. The velocity component unaffected by the wing shock was added to the predicted velocity within the flow field. The resultant velocities were used to obtain local Mach number and impact-pressure distributions through the flow field.

The predicted Mach number and static-pressure values through the flow field for the wing are presented in figure 13 at the two Mach numbers of the wind-tunnel tests, $M_\infty = 5.0$ and 8.0 . Normalized static-pressure values from the surface to the shock at selected chord locations for $\frac{x}{r}$ from 10 to 187 are presented in figure 13(a). The detached leading-edge shock causes large gradients in the static-pressure distribution through the flow field near the leading edge, for example, at $\frac{x}{r} = 10$. The effect of the shock on the pressures diminishes rapidly with increasing $\frac{x}{r}$. This results in a decrease in the gradient through the flow field, at a given Mach number. The effect of increasing Mach number is to generally increase the pressures at a given position in the flow field. For a given $\frac{x}{r}$ the pressure gradient also increases with Mach number.

Local Mach number values from the surface to the shock are presented in figure 13(b). The local Mach numbers through the flow field show a general increase in level with increasing chord length and free-stream Mach number. The increase in magnitude results from the expansion of the flow around the airfoil section. The relatively large variation in Mach number near the surface, below $\frac{z}{r} \approx 10$, results from the total-pressure variation in this region. The detached shock wave produces a total-pressure variation in the inviscid flow field resulting from the rapidly changing shock angle near the stagnation region.

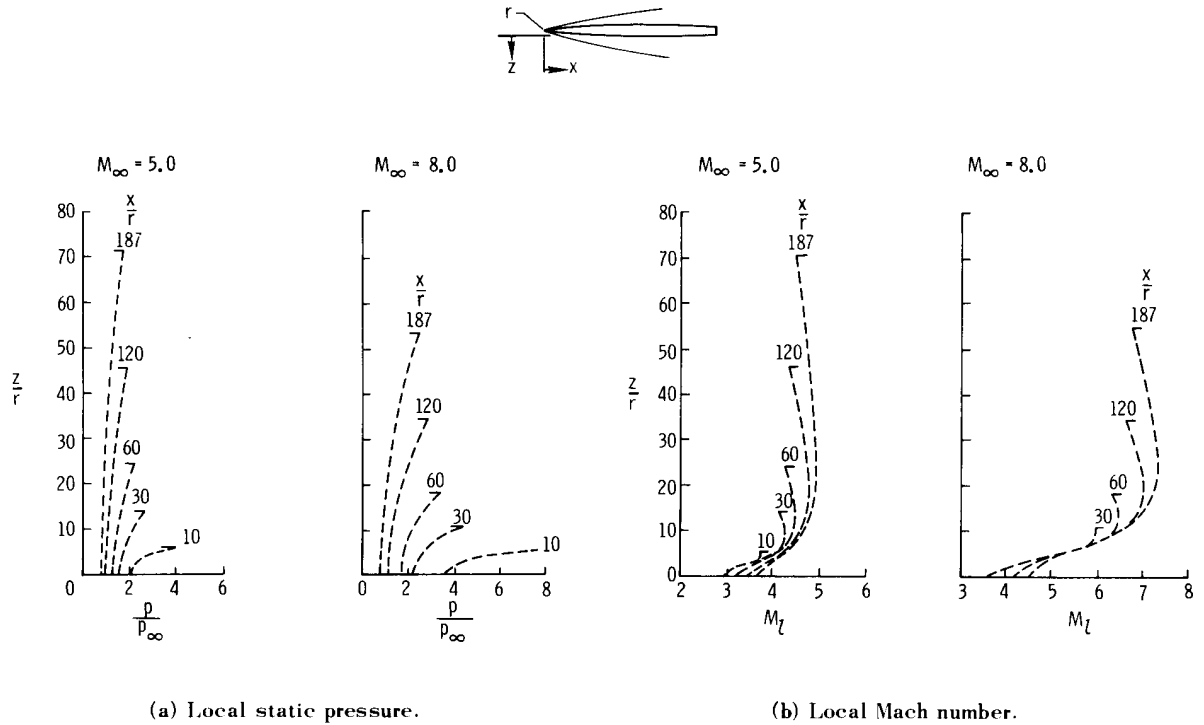


Figure 13.— Variation of Mach number and static pressure along the wing surface at $\alpha = 0^\circ$ as predicted by the Inouye-Lomax solution.

Wind-tunnel surveys.— The wing of the X-15 is partially immersed in the flow field of the body. The position of the bow shock relative to the wing is shown in figure 14. The bow-shock position is shown at two Mach numbers for which schlieren data are available. Also shown in the figure are the two span positions at which impact pressures were obtained. As can be seen, the 66-percent semispan is within the flow field of the body for both Mach numbers, whereas the 91-percent-semispan position is outside the bow shock for free-stream Mach numbers greater than 6.9.

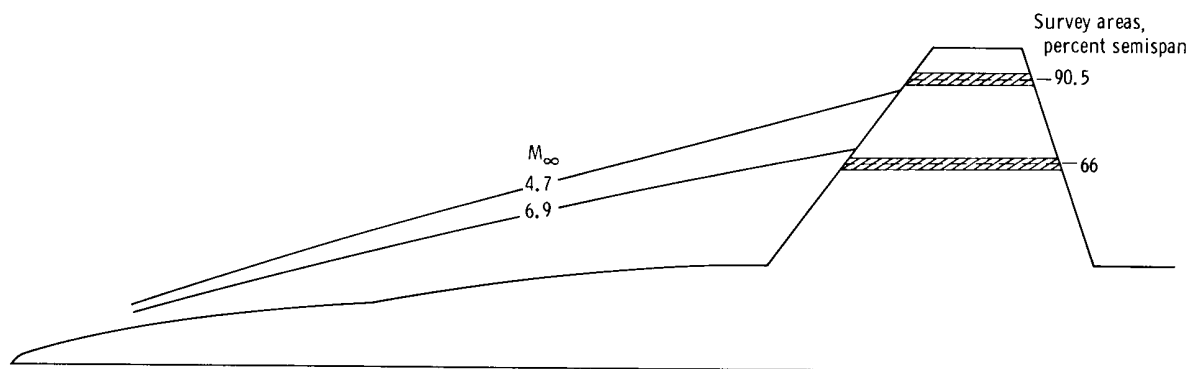
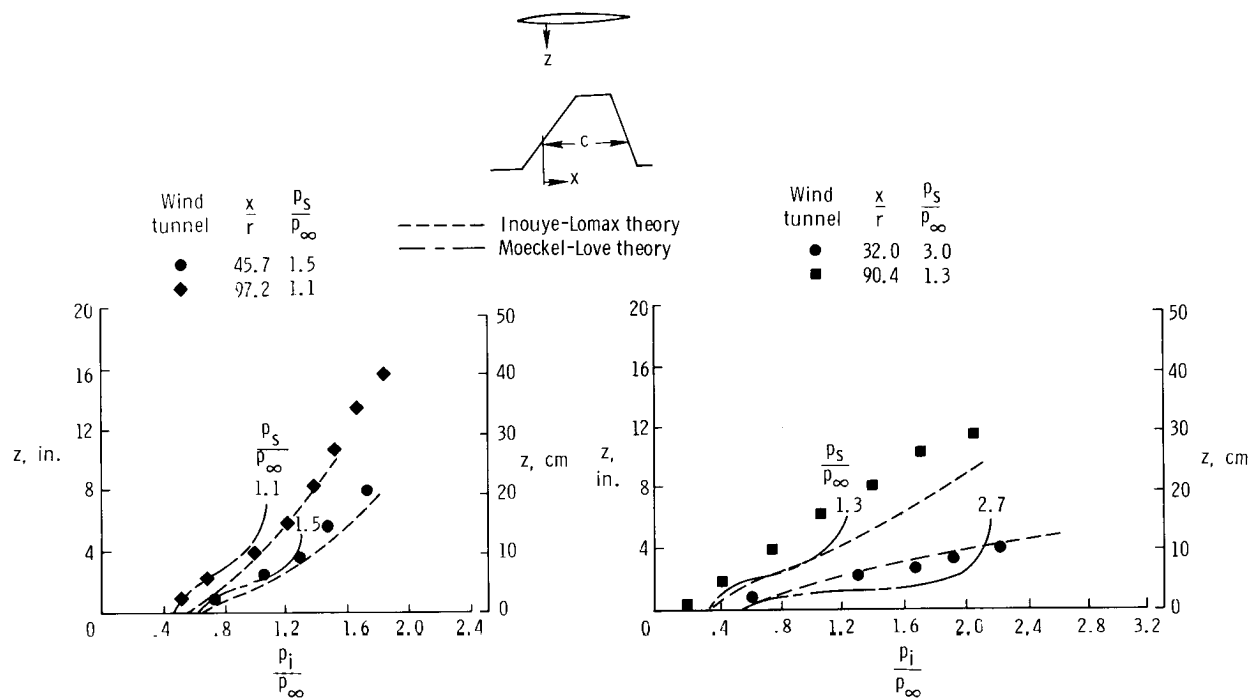


Figure 14.— Location of the survey areas on the wing lower surface relative to the bow shocks of the wind-tunnel model at $\alpha = 0^\circ$.

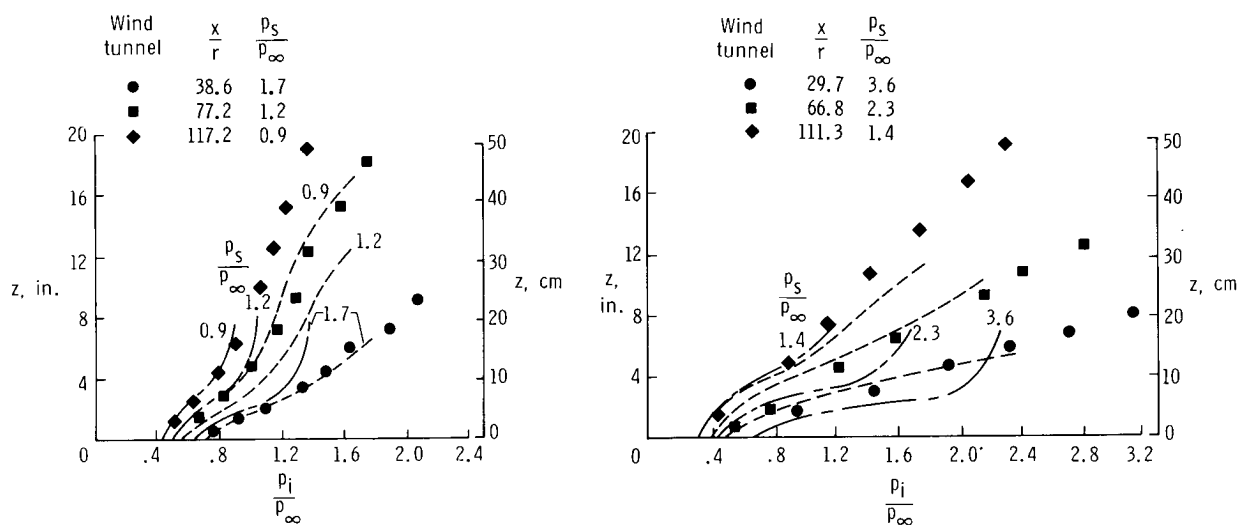
Normalized impact pressures from the wing lower surface through the flow field along both test positions for $\alpha = 0^\circ$ are presented in figures 15(a) to 15(d). The data, obtained at several chord positions at $M_\infty = 5.0$ and 8.0 , are compared with calculated results from the Inouye-Lomax and Moeckel-Love numerical procedures. The Inouye-Lomax calculations show good agreement in level and trend with the data obtained at the first chord position along the outboard row (figs. 15(a) and 15(b)). The deviation in agreement between calculations and measurements beyond this chord position is attributed partially to disturbances arising from the wing tip. The measurements along the inboard row are also compared with these calculations (figs. 15(c) and 15(d)). This row is within the flow field of the body at both Mach numbers; nevertheless, good agreement is shown in level and trend at the first chord station. Although a reduction in Mach number (see fig. 4(a)) occurs forward of this row (ahead of the wing), it is thought that the increase in static pressure within the body flow field has a compensating effect on the local impact pressures. A divergence in level between the measurements and the Inouye-Lomax calculations occurs with increasing distance downstream. However, the trend of the theory appears to follow the trend of the measurements through the flow field.

The Moeckel-Love calculations based on the measured surface static pressure and free-stream Mach number show good agreement in level with the measurements up to approximately 4 inches (10.16 centimeters) from the surface at both test rows. The values for the Moeckel-Love calculations reach a plateau at about $z = 4$ inches (10.16 centimeters), whereas the Inouye-Lomax values increase. The Moeckel-Love calculations assume a constant static pressure through the flow field, but the Inouye-Lomax method calculates a new static pressure at each height below the wing surface. Greater deviation between the Moeckel-Love calculations and the measurements exists at $M_\infty = 8.0$ than at $M_\infty = 5.0$.



(a) 90.5-percent semispan, $M_\infty = 5.0$.

(b) 90.5-percent semispan, $M_\infty = 8.0$.



(c) 66-percent semispan, $M_\infty = 5.0$.

(d) 66-percent semispan, $M_\infty = 8.0$.

Figure 15.— Comparison of wind-tunnel impact-pressure distribution through the flow field of the wing lower surface with calculations at $\alpha = 0^\circ$ and $M_\infty = 5.0$ and 8.0 .

Normalized impact pressure as a function of angle of attack is presented in figures 16(a) and 16(b) for $M_\infty = 5.0$ and 8.0 , respectively. The data were obtained at the 79-percent chord of the inboard row. The calculations from the Moeckel-Love numerical procedure are compared with the measured data. As shown, the Moeckel-Love calculations agree with the measured data for $M_\infty = 5.0$ at $\alpha = 0^\circ$ and 10° up to approximately 4 inches (10.16 centimeters) from the surface. Greater deviation exists between the measured and calculated values at $M_\infty = 8.0$ than at $M_\infty = 5.0$, partly because of the effect of the bow shock on the flow. There appears to be an embedded shock affecting the flow at this location, as shown by the sharp discontinuities in the flow at $\alpha = 10^\circ$ and 20° . This discontinuity probably results from the interaction of the bow shock and the wing shock.

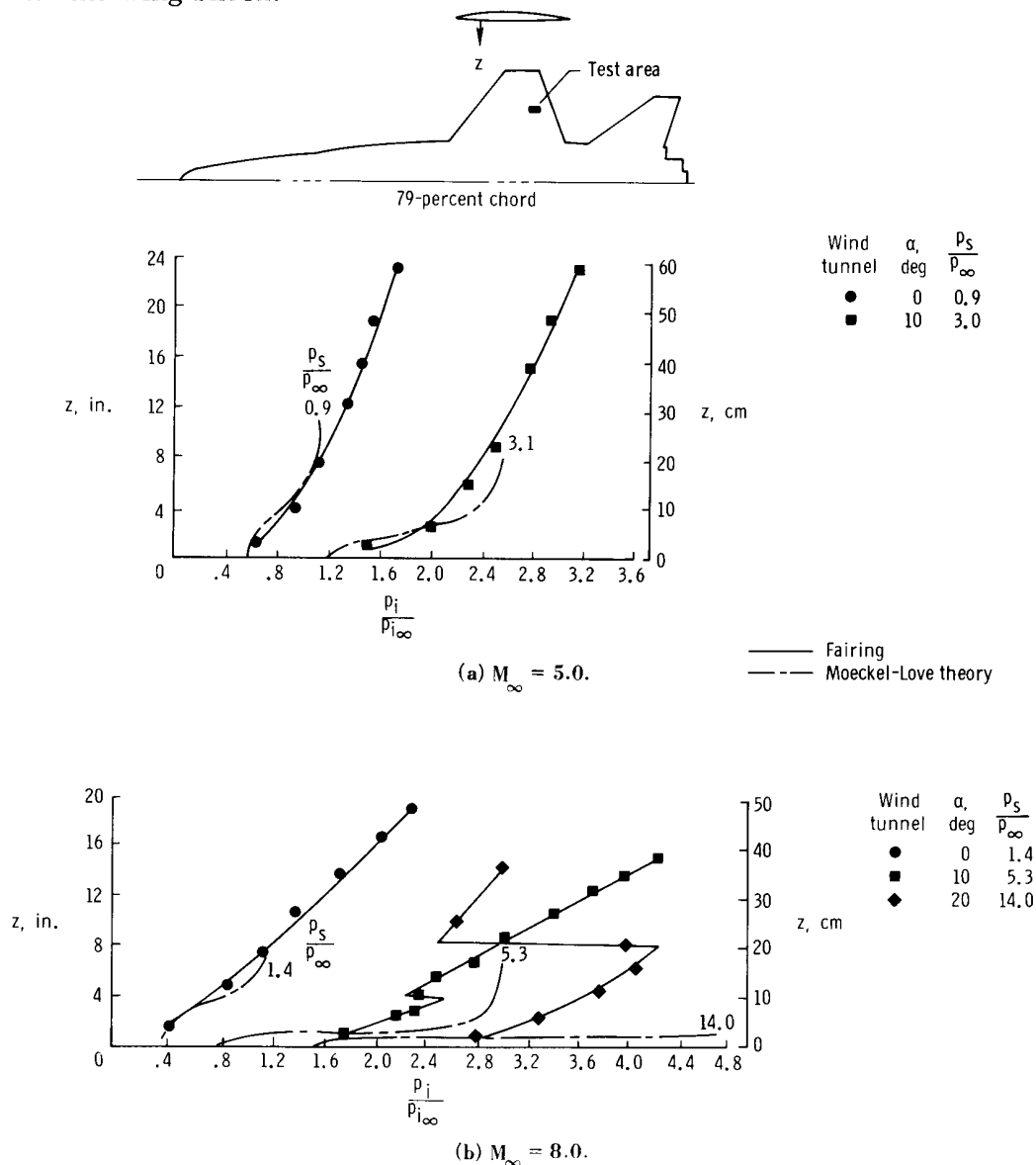


Figure 16.— Effect of angle of attack on the wind-tunnel impact-pressure distribution through the flow field of the wing lower surface at the 66-percent-semispan position.

Flight surveys.— A rake at the 73-percent chord of the survey area was used to obtain impact-pressure measurements up to 4.0 inches (10.16 centimeters) from the lower surface of the wing. Normalized impact-pressure values obtained in flight on the wing are presented in figure 17 at constant heights below the surface over the angle-of-attack range of -2° to 13° . The flight data are compared with wind-tunnel values at $M_\infty = 4.7$ and 5.0 and show good agreement over the angles of attack covered.

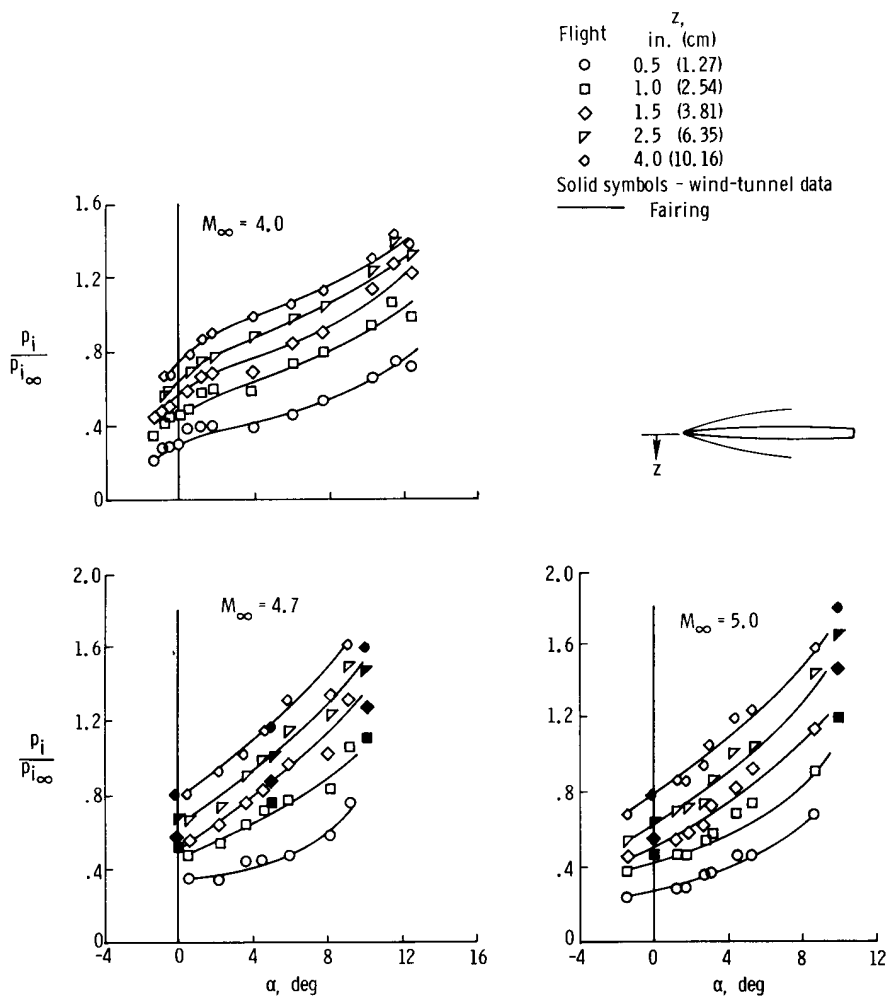


Figure 17.— Effect of angle of attack on the normalized impact pressures obtained in flight and wind-tunnel tests on the wing lower surface.

Local Mach numbers derived from the surface static pressures and rake impact pressures are presented in figures 18(a) and 18(b) for free-stream Mach numbers from 2.4 to 5.5 at two representative angles of attack, 0° and 10° . The flight data are compared with the Moeckel-Love predictions by assuming the free-stream Mach number in front of the wing and using the local surface static pressure which is assumed to be constant through the flow field. Good agreement between the measured and predicted values is shown at both angles of attack up to $M_\infty = 5.5$ beyond 1 inch (2.54 centimeters) from the surface. Predictions of the Inouye-Lomax theory at $M_\infty = 4.7$ and 5.0 are also presented in figure 18(a) at $\alpha = 0^\circ$ for comparison with the flight data.

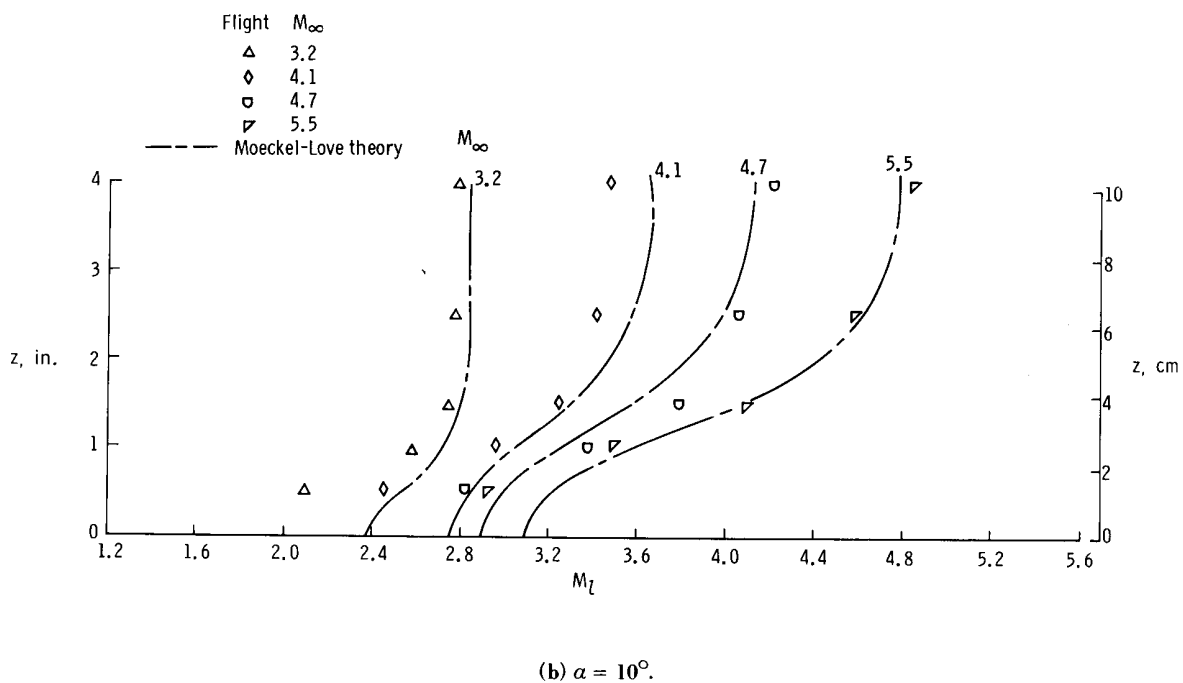
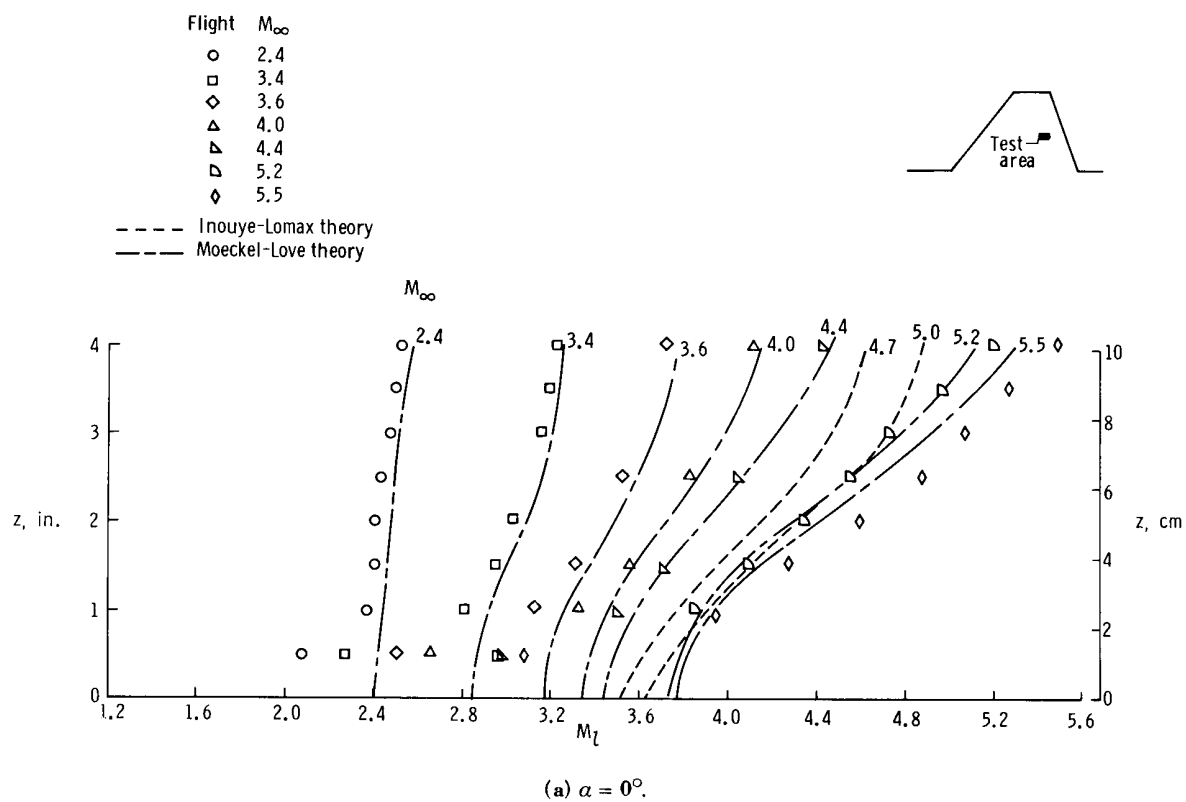


Figure 18.— Local Mach number variation on the wing lower surface in flight at $\alpha = 0^\circ$ and 10° .

CONCLUSIONS

Flow-field measurements near the rear-lower-fuselage surface, upper vertical tail, and lower surface of the right wing of the X-15 airplane and model were compared with calculated predictions. The following conclusions were reached:

1. The calculated predictions of Inouye-Lomax and Moeckel-Love gave reasonable estimates of the flow-field parameters in the three local-flow regions. Some of the deviation in the fuselage region between wind-tunnel data and theory was due to embedded shock waves that were not accounted for by theory.
2. Flight-measured lower-fuselage impact-pressure measurements were somewhat lower than wind-tunnel measurements at a free-stream Mach number of 4.0 but the values tended to agree at higher Mach numbers. The general level of the flight data agreed with the Inouye-Lomax solution for zero angle of attack.
3. Flow-field impact pressures measured on the vertical tail fitted with both a sharp and a blunt leading edge were in general agreement with wind-tunnel data. The chordwise effect on the impact pressures measured on the blunt-leading-edge vertical tail was not seen in the sharp-leading-edge vertical-tail data.
4. Dynamic pressures measured on the leading edge of the upper vertical tail in flight decreased with increasing angle of attack and increasing hypersonic Mach numbers. These trends with increasing angle of attack are attributed to the blanketing effect of the forward fuselage and canopy. The trend with increasing Mach number is attributed to the stronger bow and canopy shocks.
5. Flight and wind-tunnel impact-pressure measurements on the lower surface of the wing showed good agreement at free-stream Mach numbers of 4.7 and 5.0.

Flight Research Center,
National Aeronautics and Space Administration,
Edwards, Calif., March 22, 1968,
719-01-00-03-24.

APPENDIX

DYNAMIC-PRESSURE APPROXIMATION

The normalized impact-pressure values can be shown to approximate normalized dynamic pressures by the following relationships.

Starting with the dynamic-pressure equation

$$q = 0.7\rho M^2 \text{ (for } \gamma = 1.4 \text{)}$$

the following ratio between local and free-stream dynamic pressure is obtained:

$$\frac{q_l}{q_\infty} = \frac{p_l}{p_\infty} \left(\frac{M_l}{M_\infty} \right)^2 \quad (1)$$

Then, by using the Rayleigh pitot equation (from ref. 26)

$$p = p_i \left(\frac{6M^2}{5} \right)^{-\frac{7}{2}} \left(\frac{6}{7M^2 - 1} \right)^{-\frac{5}{2}}$$

the following equation relating impact-pressure ratio to static-pressure ratio is derived:

$$\frac{p_l}{p_\infty} = \frac{p_{i_l}}{p_{i_\infty}} \left(\frac{M_l^2}{M_\infty^2} \right)^{-\frac{7}{2}} \left(\frac{7M_\infty^2 - 1}{7M_l^2 - 1} \right)^{-\frac{5}{2}} \quad (2)$$

Substitute equation (2) into equation (1) as follows:

$$\frac{q_l}{q_\infty} = \left[\frac{p_{i_l}}{p_{i_\infty}} \left(\frac{M_l^2}{M_\infty^2} \right)^{-\frac{7}{2}} \left(\frac{7M_\infty^2 - 1}{7M_l^2 - 1} \right)^{-\frac{5}{2}} \right] \left(\frac{M_l}{M_\infty} \right)^2$$

Then, combine terms and simplify to give the following final relationship between impact pressures and dynamic pressures:

$$\frac{q_l}{q_\infty} = \frac{p_{i_l}}{p_{i_\infty}} \left(\frac{7 - \frac{1}{M_l^2}}{7 - \frac{1}{M_\infty^2}} \right)^{\frac{5}{2}}$$

An analysis of the deviation between $\frac{q_l}{q_\infty}$ and $\frac{p_{i_l}}{p_{i_\infty}}$ shows that for local Mach numbers greater than 2.0, the normalized impact pressures will be within 7 percent of the dynamic-pressure ratio.

REFERENCES

1. Pyle, Jon S. : Comparison of Flight Pressure Measurements With Wind-Tunnel Data and Theory for the Forward Fuselage of the X-15 Airplane at Mach Numbers From 0.8 to 6.0. NASA TN D-2241, 1964.
2. Pyle, Jon S. : Flight-Measured Wing Surface Pressures and Loads for the X-15 Airplane at Mach Numbers From 1.2 to 6.0. NASA TN D-2602, 1965.
3. Pyle, Jon S. : Flight Pressure Distributions on the Vertical Stabilizers and Speed Brakes of the X-15 Airplane at Mach Numbers From 1 to 6. NASA TN D-3048, 1965.
4. Hodge, B. Leon; and Burbank, Paige B. : Pressure Distribution of a 0.0667-Scale Model of the X-15 Airplane for an Angle-of-Attack Range of 0° to 28° at Mach Numbers of 2.30, 2.88, and 4.65. NASA TM X-275, 1960.
5. Osborne, Robert S. ; and Stafford, Virginia C. : Basic Pressure Measurements on a 0.0667-Scale Model of the North American X-15 Research Airplane at Transonic Speeds. NASA TM X-344, 1960.
6. Aerodynamic Projects: Pressure Distributions on the .0667-Scale Pressure-Heat Transfer Model of the X-15 Airplane at Mach Numbers From 0.60 to 7.0. Rep. No. NA-59-1362, Vols. I-V, North American Aviation, Inc. , 1959.
7. Palitz, Murray: Measured and Calculated Flow Conditions on the Forward Fuselage of the X-15 Airplane and Model at Mach Numbers From 3.0 to 8.0. NASA TN D-3447, 1966.
8. Quinn, Robert D. ; and Palitz, Murray: Comparison of Measured and Calculated Turbulent Heat Transfer on the X-15 Airplane at Angles of Attack Up to 19.0° . NASA TM X-1291, 1966.
9. Banas, Ronald P. : Comparison of Measured and Calculated Turbulent Heat Transfer in a Uniform and Nonuniform Flow Field on the X-15 Upper Vertical Fin at Mach Numbers of 4.5 and 5.3. NASA TM X-1136, 1965.
10. Pack, R. L. : The Geometric and Aerodynamic Local Flow Characteristics of the X-15 Research Airplane. Rep. No. NA-62-1334, North American Aviation, Inc. , Dec. 21, 1962.
11. Rippey, J. : Flow-Field Investigation of a 0.0667-Scale Model of the X-15 Research Vehicle at Mach 4, 6, and 8. Tech. Doc. Rep. No. AEDC-TDR-64-201, Arnold Eng. Dev. Center, Oct. 1964.
12. Montoya, Earl J. ; and Palitz, Murray: Wind-Tunnel Investigation of the Flow Field Beneath the Fuselage of the X-15 Airplane at Mach Numbers From 4 to 8. TM X-1469, 1967.

13. Wolowicz, Chester H.; and Gossett, Terrence D.: Operational and Performance Characteristics of the X-15 Spherical, Hypersonic Flow-Direction Sensor. NASA TN D-3070, 1965.
14. Gracey, William: Wind-Tunnel Investigation of a Number of Total-Pressure Tubes at High Angles of Attack. Subsonic, Transonic, and Supersonic Speeds. NACA Rept. 1303, 1957. (Supersedes NACA TN 3641.)
15. Larson, Terry J.; and Webb, Lannie D.: Calibrations and Comparisons of Pressure-Type Airspeed-Altitude Systems of the X-15 Airplane From Subsonic to High Supersonic Speeds. NASA TN D-1724, 1963.
16. Webb, Lannie D.: Characteristics and Use of X-15 Air-Data Sensors. NASA TN D-4597, 1968.
17. Anon.: Test and Model Information for Wind Tunnel Tests of an 0.02-Scale Model of the X-15 Research Vehicle in the JPL 20-Inch Supersonic Wind Tunnel. Rep. No. NA-63-636, North American Aviation, Inc., May 29, 1963 (rev. June 6, 1963).
18. Anon.: Manual for Users of the Unitary Plan Wind Tunnel Facilities of the National Advisory Committee for Aeronautics. NACA, 1956.
19. Anon.: Test Facilities Handbook. Fifth ed., vol. 4, Arnold Eng. Dev. Center, July 1963.
20. Inouye, Mamoru; and Lomax, Harvard: Comparison of Experimental and Numerical Results for the Flow of a Perfect Gas About Blunt-Nosed Bodies. NASA TN D-1426, 1962.
21. Fuller, Franklyn B.: Numerical Solutions for Supersonic Flow of an Ideal Gas Around Blunt Two-Dimensional Bodies. NASA TN D-791, 1961.
22. Gallo, William F.; and Rakich, John V.: Investigation of Methods for Predicting Flow in the Shock Layer Over Bodies at Small Angles of Attack. NASA TN D-3946, 1967.
23. Quinn, Robert D.; and Kuhl, Albert E.: Comparison of Flight-Measured and Calculated Turbulent Heat Transfer on the X-15 Airplane at Mach Numbers From 2.5 to 6.0 at Low Angles of Attack. NASA TM X-939, 1964.
24. Moeckel, W. E.: Some Effects of Bluntness on Boundary-Layer Transition and Heat Transfer at Supersonic Speeds. NACA Rept. 1312, 1957. (Supersedes NACA TN 3653.)
25. Love, Eugene S.: A Reexamination of the Use of Simple Concepts for Predicting the Shape and Location of Detached Shock Waves. NACA TN 4170, 1957.
26. Ames Research Staff: Equations, Tables, and Charts for Compressible Flow. NACA Rept. 1135, 1953. (Supersedes NACA TN 1428.)